Alignment of fractures on Bennu's boulders indicative of rapid asteroid surface evolution

Marco Delbo, Kevin Walsh, Christophe Matonti, Justin Wilkerson, Maurizio Pajola, Manar Al Asad, Chrysa Avdellidou, Ronald-Louis Ballouz, Carina Bennett, Harold Connolly, et al.

Alignment of fractures on Bennu's boulders indicative of rapid asteroid surface evolution

Marco Delbo[1], Kevin J. Walsh[2], Christophe Matonti[3], Justin Wilkerson[4], Maurizio Pajola[5], Manar M. Al Asad[6], Chrysa Avdellidou[1], Ronald-Louis Ballouz[7], Carina A. Bennett[7], Harold C. Connolly Jr.[8,7], Daniella N. DellaGiustina[7], Dathon R. Golish[7], Jamie L. Molaro[9], Bashar Rizk[7], Stephen R. Schwartz[7,9], and Dante S. Lauretta[7]

[1] Université Côte d'Azur, CNRS, Observatoire de la Côte d'Azur, Laboratoire Lagrange, Nice, France.

[2] Southwest Research Institute, Boulder, Colorado, USA.

[3] Université Côte d'Azur, CNRS, Observatoire de la Côte d'Azur, Géoazur, Sophia-Antipolis Valbonne, France.

[4] J. Mike Walker '66 Department of Mechanical Engineering, Texas A&M University, College Station, Texas, USA.

[5] Istituto Nazionale di Astrofisica, Osservatorio Astronomico di Padova, Padova, Italy.

[6] Department of Earth, Ocean and Atmospheric Sciences, University of British Columbia, Vancouver, British Columbia, Canada.

[7] Lunar and Planetary Laboratory, University of Arizona, Tucson, Arizona, USA.

[8] Department of Geology, School of Earth & Environment, Rowan University, Glassboro, New Jersey, USA.

[9] Planetary Science Institute, Tucson, Arizona, USA.

On asteroids, fractures develop due to stresses driven by diurnal temperature variations at spatial scales ranging from sub-millimetres to meters. However, the timescales of such rock fracturing by thermal fatigue are poorly constrained by observations. Here we analyse images of the asteroid (101955) Bennu obtained by the OSIRIS-REx mission and show that meter-scale fractures on the boulders exposed at the surface have a preferential meridional orientation, consistent with cracking induced by diurnal temperature variations. Using an analytical model of fracture propagation, we suggest that fractures the length of those on Bennu's boulders can be produced in 10^4 - 10^5 years. This is a comparable or shorter timescale than mass movement processes that act to expose fresh surfaces and reorient boulders and any preferential direction signature. We propose that boulder surface fracturing happens rapidly compared to the lifetime in near-Earth space of Bennu and other carbonaceous asteroids. The damage due to this space weathering process has consequences for the material properties of these asteroids, with implications for the preservation of the primordial signature acquired during the accretional phases in the protoplanetary disk of our solar system.

Low-albedo asteroids, such as the parent body of the ∼500-m-diameter (101955) Bennu, are thought to have accreted in the protoplanetary disk (∼4.56 Gyr ago) from primitive materials rich of volatile, prebiotic, and organic compounds[1]. Organics have indeed been detected on Bennu[2,3] by means of NASA's Origins, Spectral Interpretation, Resource Identification, and Security–Regolith Explorer (OSIRIS-REx)[4] mission. On 20 October 2020, OSIRIS-REx collected samples from a site called Nightingale on Bennu's surface to return to Earth[5].

Studies show that Bennu – like other small ($\lesssim$ 10 km) asteroids – formed in the main belt from the re-accumulation[6] of debris produced by the collisional fragmentation of a larger parent asteroid. During this process, primitive materials, once protected inside the parent body, may have ended up[6] on

Bennu's surface, thus becoming exposed to space weathering processes[7]. The intensities and timescales of these phenomena must be addressed in order to understand the primitiveness of the samples and of the surface where they were collected, as well as asteroid surface evolutionary processes.

One such process is material damage due to thermal fatigue[8,9,10]. This consists of the propagation of fractures driven by the mechanical stresses generated by the temperature variations[11] between day and night. Evidence of this process is growing from the study of planets such as Earth[12] and Mars[13]. On asteroids, this evidence comes from the observations of exfoliation sheets on several boulders on Bennu[10], and some boulder fractures observed[14] by JAXA's Hayabusa2 mission on (162173) Ryugu, a similarly low-albedo, kilometre-sized asteroid. Moreover, many boulders on Bennu also display meter-long fractures[4,15], whose origin and growth timescales are unknown.

The most unambiguous evidence of thermal fatigue driven by diurnal temperature cycles would be a preferred approximately North-South orientation[12,13,16,17] of fractures. We should expect to see this on Bennu's boulders because their cyclical exposure to the Sun on their East side in the morning and West side in the afternoon generates non-linear temperature gradients[18,19] producing thermal stresses with the same orientation[17,16], which drive fracture propagation approximately in the perpendicular direction (North-South). We used OSIRIS-REx observations to determine the directions of fractures on Bennu's boulders and assess whether they were formed by this mechanism.

Identification and mapping of fractures

Using mosaics[20] of images of Bennu's surface obtained by the OSIRIS-REx PolyCam[21] with a resolution of ∼5 cm pixel^{-1}, we visually identified 1,528 fractures (Methods) in the latitude (ϕ) range $-50° < \phi < +50°$ (Fig. 1, Extended Data Fig. 1–2). Each fracture was manually mapped by drawing a poly-line from the beginning to the end of the fracture. Fractures are thus represented by a total of 3,215 segments. The reliability of the visual fracture identification was assessed (Methods) by mapping fractures on some higher-spatial-resolution images and by an independent fracture mapping in selected areas (Extended Data Fig. 3).

We find fractures on all types of boulders, regardless of their morphology[22] and brightness[7] (Extended Data Fig. 4). Some fractures are relatively straight; others display irregular shapes that develop along angular broken lines, whose segments connect in general with angle <90° (Fig. 1a). Merging fractures can form crudely shaped polygonal networks, which have been interpreted previously on other small bodies[23] to result from thermal stresses (Fig. 1a,b). The general angular and broken line-like shape of fractures is compatible with opening-mode, low-stress, and low-confinement fracture formation and propagation conditions[24]. These are typically generated by stresses driven by surface diurnal temperature cycles, which slowly propagate fractures, in sub-critical stress regimes[19,18]. Some well-defined fractures span the entire length of the boulder (Fig. 1c), whereas others affect only a small portion of their host boulder (Fig. 1d). Some other fractures are less obvious and could be confused with layers in the boulder fabric (Fig. 1e). We also observe through-going fractures, which appear to break and split the hosting boulder (Fig. 1f,g). Examples of boulders with morphologies consistent with in situ breakdown have been previously described in lower-spatial-resolution observations[4,15] and are mapped here with higher spatial resolution (Fig. 1g). Particularly difficult is the unambiguous identification of fractures on hummocky boulders[22] (Fig. 1h,i). It is also not always obvious whether the different segments of what we mapped as a single fracture are in reality separate ones. For this reason, we proceed with further analysis both on fractures and on fracture segments.

Figure 2 shows that the distribution of the fracture and fracture segment orientations (Methods) is non-random, with a preferential direction approximately North-West to South-East, independently of the latitude on the asteroid, surface boulder density, and fracture mapping method (Extended Data Fig. 5). We performed a Kolmogorov-Smirnov test against the null hypothesis that the directions of the fracture segments and of the fractures are drawn from a uniform distribution. We find p-values $<10^{-20}$, indicating that we can reject the null hypothesis at $\gg$99.99% confidence. The preferred fracture orientation is very unlikely to be due to fracture detection and mapping biases (Methods), because the former is eliminated by identifying fractures at different latitudes, while the latter would tend to enhance a East-to-West preferred fracture orientation, which is not observed. We thus conclude that the non-uniform fracture distribution is not due to random coincidence or observational biases. This preferential direction distribution is indicative of fractures driven by diurnal temperature stresses [16] and has been observed on other solar system bodies [12,13]. Following previous studies [12], the offset of the preferential direction from pure North-South can be attributed to the Sun preferentially illuminating boulders' North-East sides at time of maximum stress (morning and perihelion; Methods). This effect could have been stronger in the past, possibly due to a higher obliquity than the current one, caused by Bennu's spin axis mobility due to thermal torques [1].

Figure 2 also shows that a larger number of fractures are found in the equatorial band ($-15° < \phi < 15°$) compared to the northern ($15° < \phi < 50°$) and southern ($-50° < \phi < -15°$) mid-latitudes. When we normalise (Methods) the latitudinal fracture occurrence by the latitudinal boulder frequency [7] (there are more boulders at mid-latitudes than in the equatorial band), the excess of equatorial fractures compared to mid-latitude ones increases (Extended Data Fig. 6). This is another indication of a thermal stress-driven origin of fractures: Fracture propagation rate is positively correlated with the amplitude of the temperature excursion between day and night [8,19], which is larger at the equator than at the mid-latitudes because the spin axis of Bennu is almost perpendicular to its orbital plane [4].

Figure 3 shows that the length distributions of fracture and fracture segments (Methods) fit an exponential law. This type of distribution was previously noted for the polygonal fractures observed on the nucleus of comet 67P Churymov-Gerasimenko, and interpreted to have a thermal stress-driven origin [25,23]. This is because opening-mode fracture propagation in a confined medium can result in a length distribution that follows an exponential law [26]. For lengths $\gtrsim$4 m, we observe that the length distribution of fractures follows a power law (Fig. 3). This could be related to the fact that $\gtrsim$4 m-long fractures have lengths comparable to the sizes of the hosting boulders. In this case, fracture length follows the size distribution of boulders, which is known to be represented by a power law [22]. This is also indicated by the value of the power law exponent that we derived for the fracture lengths, -2.4 ± 0.4 (Fig. 3), which is similar to the one determined [22] for boulder sizes (-2.9 ± 0.3). Moreover, because the spatial resolution of the images ($\sim$5 cm pix^{-1}; Methods) is about six times smaller than the shortest mapped fracture (Fig. 3), it is likely that the roll-off below 2 m of the distribution of fracture lengths compared to a power law is due to the fracturing mechanism and unlikely caused by a bias against the mapping of small fractures (i.e. a censoring effect).

Meteoroids impact asteroids [14,27], thereby fracturing boulders [14]. However, impact-driven fractures on a uniform boulder surface should not follow a preferred orientation, but rather a centrosymmetric radial distribution [14,28]. This has been observed on lunar rocks [28], Ryugu [14], Bennu (Extended Data Fig. 7), and on laboratory impact experiments on simulants of low-albedo asteroidal boulders [29]. These experiments also show that when the material is non-uniform, the directions of the impact-driven fractures are constrained by the heterogeneities. Because there is no reason to assume that boulders

on asteroids have heterogeneities directed North-West to South-East, we argue that impacts cannot be the source of the preferred orientation of fractures on Bennu.

In conclusion, the orientation, latitude, and length distributions of fractures on Bennu's boulders all point to a thermal fatigue origin, in general. However, impacts can also contribute to boulder fracturing on Bennu, explaining some fractures oriented otherwise than North-West to South-East (Fig. 2).

Timescale of thermal fatigue fracturing

Using established methods[8,18,19] we developed a model (Methods; Extended Data Fig. 8) to calculate the time it takes for the thermal fatigue to propagate a fracture vertically, into the boulder mass[8,18,19], as well as horizontally along the boulder surface[16]. We found that it can take several millions of years for a fracture to penetrate vertically through boulders with sizes of a few meters (Methods). On the other hand, our model predicts that fractures propagate horizontally with a rate some tens to hundreds of times faster than vertically. Hence, a size distribution of initially microscopic surface fractures can grow in length to a few meters (comparable to the fracture lengths in Fig. 3) in a timeframe between about 10,000 and 100,000 years (Extended Data Fig. 9). Typical uncertainties of calculated fracture propagation rates are about one order of magnitude (Methods and Extended Data Tab. 1).

Surface morphologies indicative of mass movement on Bennu have been identified and estimated to have occurred within the past few hundreds of thousands of years[30]. Mass movement would lead to (i) the exposure of fresh boulder faces and (ii) re-orientation of already exposed boulder faces. In the case of (i), thermal cracking would create new fractures with preferred North-West to South-East direction. In the case of (ii), we would expect there to be no preference in the orientation. Our observations point to the case (i) and, combined with our model, indicate that thermal fracturing is a fast process, developing in a timescale shorter or comparable to those of the last mass movement and certainly shorter than Bennu's lifetime (1.75 Myr) in near-Earth space[27].

Implications for asteroid surface evolution

The faster horizontal rate of fracture propagation compared to vertical, driven by diurnal temperature changes, determines that fractures are long relative to their depth, as often is observed (Fig. 1). This is also consistent with laboratory experiments, where thermal fatigue was induced in a CM carbonaceous chondrite meteorite – a good analogue of Bennu's composition[3] – by means of radiative heating[31] (despite at a smaller spatial scale, compared to the fractures observed here).

Material damage increases with increasing time, because fractures increase their lengths (Extended Data Fig. 9), and more slowly also their depths. Pervasive fractures can decrease materials' thermal conductivity[32], thus, contributing to explain the lower thermal inertia of boulders on Bennu[11] and Ryugu[33,34,35] compared to those of meteorites[33].

The surface and sub-surface of boulders that have been exposed to a larger number of diurnal temperature cycles would be more damaged than the underlying layers or the boulder interior, creating a strength dependence with depth or stratification. Impacts on targets with strength stratification result in flat-bottom or concentric craters[36], showing benched profiles. Craters with flat-bottom profiles exist on Bennu's boulders (e.g., ref.[27] Fig. 2), while a crater with a concentric profile is shown in Extended Data Fig. 7, providing further evidence for the strength stratification of boulders by

thermal fatigue. One would also expect craters' depth to diameter ratio to decrease with increasing diameter on boulders with strength stratification, because larger craters excavated deeper and stronger material[27]. However, this trend might be non-trivial to observe because the two primary types of boulders on Bennu[7] have different thermal inertia (implying different porosities and strength)[11] and different size distributions[7].

The fatigue driven by diurnal temperature changes can be seen as a space weathering process on asteroid surfaces, whereby they progressively lose their primordial thermo-mechanical properties and undergo increasing material damage as the number of temperature cycles increases. Thermally weakened boulders are more easily broken down by meteoroid impacts and by thermal fatigue itself[8,10], possibly contributing to mass ejection[17], which has been observed on Bennu[37]. This process could even lead to asteroid disruption[38] at small perihelion distances. All these effects contribute to the meteoroid population, also leading to material delivery to Earth[39].

Bennu and Ryugu have higher boulder abundance compared to pre-exploration expectations[4,14], which could be a common feature[40] of the most numerous compositional type of asteroids[40]. The thermal fatigue rate depends on boulders' material[8,17,40], rotation rate[19], and heliocentric distance of the body[8,19]. For instance, on bodies with slow rotation rates, such as our Moon, meteoroid impacts appear to be the predominant boulder breakup process[28]. Given all this, understanding the thermal processes that affect boulders properties and their erosion is more important than previously thought in controlling the evolution of these small bodies.

Acknowledgments

This material is based upon work supported by NASA under contract NNM10AA11C issued through the New Frontiers Program. We are grateful to the entire OSIRIS-REx Team for making the encounter with Bennu possible, to C. Wolner for editorial help and to the OPAL infrastructure of the Observatoire de la Côte d'Azur (CRIMSON) for providing computational resources and support. M.D. and C.A. acknowledge the French space agency CNES and support from ANR "ORIGINS" (ANR-18-CE31-0014). M.P. was supported for this research by the Italian Space Agency (ASI) under the ASI-INAF agreement no. 2017-37-H.0. S.R.S. was supported by Grant no. 80NSSC18K0226 as part of the OSIRIS-REx Participating Scientist Program. We thank D. Durda for useful comments that improved our manuscript.

Author contributions

M.D. led the project, the interpretation of the results and the development of the manuscript. M.D., M.P., and M.M.A.A. mapped fractures; K.J.W. compared the independent fracture mapping. C.M. contributed to the interpretation of fractures. J.W. and M.D. developed the thermal fatigue fracture mechanics model, which was discussed with and improved by J.M. D.D.G., C.B., D.G. provided image processing support. M.D., K.J.W. wrote codes for the analysis. C.A., R-L.B., H.C.C., C.B., D.D.G., D.G., J.M., B.R., S.R.S., and K.J.W. provided support in the interpretation of spacecraft imagery. C.A. and R-L.B. helped with comparison against impact driven fractures. K.J.W. and B.R. contributed to the data interpretation during the OSIRIS-REx Regolith Development Working Group (RDWG) and Image Processing Working Group (IPWG) meetings, and to design of the observations and data acquisition. K.J.W. and D.D.G. led the RDWG and the IPWG, respectively. D.S.L. made

this study possible as the PI of the OSIRIS-REx mission and contributed to the discussion of the results. M.D., C.M., and K.J.W. wrote the manuscript with contribution of text, figures, equations, and discussions from all coauthors.

Competing interest declaration

The authors declare no competing interests.

Figure Legends/Captions (for main text figures)

Figure 1

Examples of different fracture morphologies and fracture mapping. (a,b) Fracture networks. (c) Through-going fracture. (d) Fracture affecting only part of the hosting boulder. (e) layer-like fractures. (f,g) Through-going fractures appearing to split the boulders. (h,i) Fractures on hummocky boulders. The red poly-lines represent the mapped fractures and their segments. Extended Data Fig. 1 presents the same panels without the mapping poly-lines allowing better visualisation of the fractures.

Figure 2

Windrose histograms of the azimuthal direction of fractures and fracture segments. The top plots (a,b,c) present the fracture directions. The bottom plots (d,e,f) display the directions of the elementary segments that compose the fractures. The diagrams are plotted for three different bands of latitude ϕ: (a,d) northern mid-latitudes; (b,e) equatorial; (c,f) southern mid-latitudes.

Figure 3:

Cumulative distribution of the length of fractures and fracture segments. The dashed-dotted curves represent best-fit exponential functions of the form $N = N_1 e^{\beta L_x}$, where L_x is the length of the fractures or of the fracture segments (abscissa) and N is their cumulative number (ordinate). We obtain $N_1 = 2525 \pm 24$, $\beta = -0.585 \pm 0.003$ for the fracture length distribution and $N_1 = 4284 \pm 12$, $\beta = -0.939 \pm 0.003$ for the fracture segment length distribution. The thick-dashed straight line is the best fit of a power-law function of type $N = N_0 L_x^{\gamma}$ for $4 \leq L_x \leq 10$ m. We find $N_0 = 6347 \pm 20$ and $\gamma = -2.4 \pm 0.4$.

References

[1] Lauretta, D. S. *et al.* The OSIRIS-REx target asteroid (101955) Bennu: Constraints on its physical, geological, and dynamical nature from astronomical observations. *Meteoritics & Planetary Science* **50**, 834–849 (2015).

[2] Simon, A. A. *et al.* Widespread carbon-bearing materials on near-Earth asteroid (101955) Bennu. *Science* **370**, abs3522 (2020).

[3] Hamilton, V. E. *et al.* Evidence for widespread hydrated minerals on asteroid (101955) Bennu. *Nature Astronomy* **3**, 332–340 (2019).

[4] Lauretta, D. S. *et al.* The unexpected surface of asteroid (101955) Bennu. *Nature* **568**, 55–60 (2019).

[5] Lauretta, D. S., Enons, H. L., Polit, A. T., Roper, H. L. & Wolner, C. W. V. Chapter 8 - OSIRIS-REx at Bennu: Overcoming challenges to collect a sample of the early Solar System. In Longobardo, A. (ed.) *Sample Return Missions: The Last Frontier of Solar System Exploration*, 163–194 (Elsevier, 2021).

[6] Michel, P. *et al.* Collisional formation of top-shaped asteroids and implications for the origins of Ryugu and Bennu. *Nature Communications* **11**, 2655–11 (2020).

[7] DellaGiustina, D. N. *et al.* Variations in color and reflectance on the surface of asteroid (101955) Bennu. *Science* **370**, eabc3660 (2020).

[8] Delbo, M. *et al.* Thermal fatigue as the origin of regolith on small asteroids. *Nature* **508**, 233–236 (2014).

[9] Molaro, J. L., Byrne, S. & Le, J. L. Thermally induced stresses in boulders on airless body surfaces, and implications for rock breakdown. *Icarus* **294**, 247–261 (2017).

[10] Molaro, J. L. *et al.* In situ evidence of thermally induced rock breakdown widespread on Bennu's surface. *Nature Communications* **11**, 2913–11 (2020).

[11] Rozitis, B. *et al.* Asteroid (101955) Bennu's weak boulders and thermally anomalous equator. *Science Advances* **6**, 41 (2020).

[12] McFadden, L. D., Eppes, M. C., Gillespie, A. R. & Hallet, B. Physical weathering in arid landscapes due to diurnal variation in the direction of solar heating. *Geological Society of America Bulletin* **117**, 161–173 (2005).

[13] Eppes, M.-C., Willis, A., Molaro, J., Abernathy, S. & Zhou, B. Cracks in Martian boulders exhibit preferred orientations that point to solar-induced thermal stress. *Nature Communications* **6**, 6712–11 (2015).

[14] Sugita, S. *et al.* The geomorphology, color, and thermal properties of Ryugu: Implications for parent-body processes. *Science* **364**, 252–252 (2019).

[15] Walsh, K. J. *et al.* Craters, boulders and regolith of (101955) Bennu indicative of an old and dynamic surface. *Nature Geoscience* **12**, 242–246 (2019).

[16] Uribe-Suárez, D., Delbo, M., Bouchard, P. O. & Pino-Muñoz, D. Diurnal temperature variation as the source of the preferential direction of fractures on asteroids: Theoretical model for the case of Bennu. *Icarus* **360**, 114347 (2021).

[17] Molaro, J. L. *et al.* Thermal Fatigue as a Driving Mechanism for Activity on Asteroid Bennu. *Journal of Geophysical Research: Planets* **125**, e06325 (2020).

[18] El Mir, C., Ramesh, K. T. & Delbo, M. The efficiency of thermal fatigue in regolith generation on small airless bodies. *Icarus* **333**, 356–370 (2019).

[19] Ravaji, B., Ali-Lagoa, V., Delbo, M. & Wilkerson, J. W. Unraveling the Mechanics of Thermal Stress Weathering: Rate-Effects, Size-Effects, and Scaling Laws. *Journal of Geophysical Research: Planets* **124**, 3304–3328 (2019).

[20] Bennett, C. A. *et al.* A high-resolution global basemap of (101955) Bennu. *Icarus* **357**, 113690 (2021).

[21] Rizk, B. *et al.* OCAMS: The OSIRIS-REx Camera Suite. *Space Science Reviews* **214**, 26 (2018).

[22] DellaGiustina, D. N. *et al.* Properties of rubble-pile asteroid (101955) Bennu from OSIRIS-REx imaging and thermal analysis. *Nature Astronomy* **3**, 341–351 (2019).

[23] Attree, N. *et al.* Thermal fracturing on comets. Applications to 67P/Churyumov-Gerasimenko. *Astronomy and Astrophysics* **610**, A76 (2018).

[24] Ragan, D. M. *Structural Geology. An Introduction to Geometrical Techniques. Fourth edition* (Cambridge University Press, 2009).

[25] Matonti, C. *et al.* Bilobate comet morphology and internal structure controlled by shear deformation. *Nature Geoscience* **12**, 157–162 (2019).

[26] Giuffrida, A. *et al.* Fracture simulation parameters of fractured reservoirs: Analogy with outcropping carbonates of the Inner Apulian Platform, southern Italy. *Journal of Structural Geology* **123** (2019).

[27] Ballouz, R. L. *et al.* Bennu's near-Earth lifetime of 1.75 million years inferred from craters on its boulders. *Nature* **587**, 205–209 (2020).

[28] Hörz, F., Basilevsky, A. T., Head, J. W. & Cintala, M. J. Erosion of lunar surface rocks by impact processes: A synthesis. *Planetary and Space Science* **194**, 105105 (2020).

[29] Avdellidou, C. *et al.* Very weak carbonaceous asteroid simulants I: Mechanical properties and response to hypervelocity impacts. *Icarus* **341**, 113648 (2020).

[30] Jawin, E. R. *et al.* Global Patterns of Recent Mass Movement on Asteroid (101955) Bennu. *Journal of Geophysical Research: Planets* **125**, 501–21 (2020).

[31] Libourel, G. *et al.* Network of thermal cracks in meteorites due to temperature variations: new experimental evidence and implications for asteroid surfaces. *Monthly Notices of the Royal Astronomical Society* **500**, 1905–1920 (2021).

[32] Hasselman, D. Effect of cracks on thermal conductivity. *Journal of Composite Materials* **12**, 403–407 (1978).

[33] Grott, M. *et al.* Low thermal conductivity boulder with high porosity identified on C-type asteroid (162173) Ryugu. *Nature Astronomy* **3**, 971–976 (2019).

[34] Okada, T. *et al.* Highly porous nature of a primitive asteroid revealed by thermal imaging. *Nature* **579**, 518–522 (2020).

[35] Shimaki, Y. *et al.* Thermophysical properties of the surface of asteroid 162173 ryugu: Infrared observations and thermal inertia mapping. *Icarus* **348**, 113835 (2020).

[36] Hörz, F. & Cintala, M. Impact experiments related to the evolution of planetary regoliths. *Meteoritics & Planetary Science* **32**, 179–209 (1997).

[37] Lauretta, D. S. *et al.* Episodes of particle ejection from the surface of the active asteroid (101955) Bennu. *Science* **366**, 3544–10 (2019).

[38] Granvik, M. *et al.* Super-catastrophic disruption of asteroids at small perihelion distances. *Nature* **530**, 303–306 (2016).

[39] Melikyan, R. E. *et al.* Bennus natural sample delivery mechanism: Estimating the flux of bennuid meteors at earth. *Journal of Geophysical Research: Planets* **126**, e06817 (2021).

[40] Cambioni, S. *et al.* Fine-regolith production on asteroids controlled by rock porosity. *Nature* **598**, 49–52 (2021).

Methods

Identification and mapping of fractures

We visually identified fractures on Bennu's boulders from images that were obtained during the Detailed Survey–Baseball Diamond Flybys 1 (hereafter FB1, ref. [41]) and 3 (hereafter FB3, ref. [20]), which occurred on 7 and 21 March, 2019, respectively. The spacecraft was positioned above Bennu's equator approximately at 12:30 PM and 10:00 AM local solar time, 4.6 and 3.46 km from the surface, and observing with phase angles of 8° and 30° during FB1 and FB3, respectively. Bennu's surface between -50° and 50° and between -70° and 70° of latitude was imaged by the OSIRIS-REx PolyCam [21] with pixel scales of ∼6.25 cm pixel^{-1} and ∼5 cm pixel^{-1} at the equator during FB1 and FB3, respectively. Emission angles at the equator were near 0°, but North/South of the equator, emission angles were higher and pixel scales were lower.

Each image was obtained with a slightly different orientation, making complicated a global survey of fractures from each single image. To overcome this limitation and keep consistency in our method, we identified fractures on global mosaics [7,20,41]. These have pixel columns and rows aligned with the latitude and the longitude.

We identified fractures as narrow lineations of pixels having low brightness that contrasts with the brightness of the underlying boulders (Fig. 1). We used the mosaic from FB3 (hereafter Mosaic-FB3) to identify the fractures and the mosaic from FB1 (Mosaic-FB1) for confirmation of the fractures. Namely, only fracture visible on both mosaics were mapped. We mapped latitudes between -50° and 50° in order to avoid regions close to the poles where the mosaics are strongly deformed

Our baseline for fracture mapping used the SAOImage DS9 computer application. In particular, Mosaic-FB3 and Mosaic-FB1 were loaded in different buffers. We used the "pan" tool to move along and across the images, making sure that both buffers were aligned, had roughly the same scale, and the active DS9 display showed the same area. With the tab key we "blinked" between the two mosaics to check for fracture visibility.

Mapping was performed by marking the longitudes and latitudes of the pixels of each fracture. Namely, one of us drew a poly-line from the beginning to the end of each fracture. For this, we used the segment tool (region→shape→segment and edit→region) of the DS9. Each fracture was thus represented by a series of adjacent "fracture segments" (Fig. 1), each of which describes a linear transformation between the (x, y) coordinates of the fracture pixels and the longitude and latitude.

We assessed the accuracy of our visual fracture identification by two methods. First, we confirmed the fractures identified on Mosaic-FB3 on higher spatial resolution (1.5 cm pixel^{-1}) images of potential sample sites considered (but not used) by the OSIRIS-REx mission: Osprey, Sandpiper, and Kingfisher, which are respectively centred at the longitudes and latitudes of (88.6°, 11.5°), (317.5°, -43.5°), and (55.8°, 11.4°). In the area covered by the higher resolution images of Osprey, we confirmed five of the six fractures identified in Mosaic-FB3 and Mosaic-FB1, while one fracture is dubious. In Sandpiper, one fracture identified from the Mosaic-FB3 and Mosaic-FB1 is visible in the higher resolution images. Likewise, we have one fracture clearly also visible in the higher resolution images of Kingfisher that we identified from the Mosaic-FB3 and Mosaic-FB1. This indicates that our visual global fracture identification is robust. In addition, more fractures than those identified from the two global mosaics are visible in the higher spatial resolution images, indicating that our baseline fracture mapping is biased against the identification of fractures smaller than some tens of centimetres. Fractures at the

Nightingale sampling site were not mapped because it is located northern than the investigated region.

The mapping described above was first performed entirely by one co-author for consistency. For verification, two other co-authors then performed a visual fracture identification and mapping independently of the first co-author. This second fracture mapping was carried out in seven areas on the surface of Bennu (Extended Data Fig. 3 and 5). These areas were selected to represent regions with diverse geological properties: e.g. higher and lower boulder density, equatorial and mid-latitude regions. This second mapping effort used the ArcGIS software package and followed a similar procedure of our baseline fracture identification using Mosaic-FB3 as reference and Mosaic-FB1 for fracture confirmation. The two mosaics were scaled and aligned using common control points. In order not to bias their respective fracture identification, the two team members did not share their results. A third co-author compared the two independent fracture identification mapping and assigned a scoring for each area. It was found that (i) the second co-author mapped slightly more fractures than the first co-author, implying that our baseline global mapping could be conservative; and (ii) the second co-author mapped 74% of the fractures also mapped by the first co-author on average across the seven selected areas, which we consider good agreement.

Orientation and length of fractures with their biases

Fracture segments azimuths are simply given by the arctan of the ratio of segments' longitude- and latitude-components. Fracture azimuth was calculated from the components of the straight line that best fits the vertices of the segments of each fracture.

The length of a fracture was taken from the sum of the lengths of its segments: First, we estimated an effective longitude and latitude of each segment taking the average of the longitudes and the average of the latitudes of the beginning and ending of each segment forming the fracture. Next, we determined the radius of the asteroid at the aforementioned effective longitude and latitude using the shape model OLA_v20.obj, which was created from laser altimetry[42]. We applied the Haversine formula between the longitude and latitude of the beginning and ending of each fracture segment, given the local asteroid radius to calculate the fracture segment length. The error in the length of the fracture is likely dominated by the human ability to map the segments. From trial and error, we estimated that this value was of the order of 3 pixels for each fracture tip, which implied a fracture length error of about $3 \times 2^{1/2}$ that we approximated to 5 pixels.

The fracture cumulative length distribution fit was performed following classic recommendations[43], namely, to have a dataset composed of more than 200 fractures ranging over almost two orders of magnitude in length. Nevertheless, for power-law fitting and interpretations, we used a conservative approach by considering a length interval far above the maximum image resolution and discarding length close to the maximum fracture size observed, in order to avoid typical issues such as: (i) the truncation effect, due to image resolution limits; (ii) the length bias or censoring effect, due to the sampling area compared to the size of longest fractures; and (iii) a statistical effect due to undersampling of the largest objects.

We crossmatched the boulder database of ref.[7] with the fractures. The former contains longitude and latitude of the centre of each boulder and the boulder radius. Using the Haversine formula, we calculated the distance between the centre of a boulder and the vertices of the segments of the fractures. We assigned a fracture to a boulder when the distances between the centre of the boulder and the vertices of the segments of the fracture were smaller than the boulder radius. Having established

the match between the fractures and the boulders, we could compare the statistics of boulders with fractures to the general statistics of boulders. Since the normal reflectance is the most diagnostic parameter to separate the boulder types[7], we plot the distribution of this parameter for boulders with fractures against the distribution of boulders in general (Extended Data Fig. 4).

To correct the number of fractures for the number of boulders in each latitude band, we proceeded as follows: (i) We counted the number of boulders in the database of ref.[7] in the three bands, namely with latitude between -50° and -15°, -15° and 15°, and 15° and 50°, and found respectively 466, 425, and 483 boulders. This means that the southern mid-latitude band has 1.10 times the number of boulders of the equatorial band, whereas the northern mid-latitude band has 1.14 times the number of boulders of the equatorial band. (ii) We counted the number of fracture segments and of fractures in each band, finding 976 fracture segments and 439 fractures between -50° and -15°of latitude, 1,222 fracture segments and 573 fractures between -15° and 15°of latitude, and 939 fracture segments and 475 fractures between 15° and 50°of latitude. (iii) We divided the count in each bin of the windrose diagrams by the equatorial number fracture segments (or fractures) and then we divided the southern and northern mid-latitude windrose diagrams by the respective factors determined at point (i). This process produced the plots in Extended Data Fig. 6.

Next, we present how we ruled out the effects of potential biases affecting fracture detection and their azimuth distribution. Fracture identification is aided by the casted shadows, making fractures directed from North to South perhaps more easily to be seen than fractures oriented East-West on boulders located at low latitudes and with faces parallel to the local surface at the equator. However, several factors reduce the effect of this bias: (a) boulders have faces, in general, titled with respect to the local surface (Fig. 1); (b) the images used to create the mosaics were taken at two different times of the day, offering different shadowing conditions; (c) we searched for and mapped fractures on boulders also at mid latitudes, northern and southern of the equator. Here, fractures extending in the East-West directions on boulders' faces having low tilt compared to the local surface should become more visible than near the equator. Concerning the direction bias, we note that the projection of images on the mosaics tends to increase their East-to-West scaling compared to their North-to-South one with increasing absolute value of the latitude. This projection scaling bias would increase the length of the East-to-West component of fracture segments with respect to their North-to-South component with increasing absolute value of the latitude. The effect of this bias is a tendency to amplify the rotation of fractures to the East-to-West azimuthal direction with increasing absolute value of the latitude. Hence, this bias would act against the measurement of a preferential direction independent of latitude, which is instead what we observed (Fig. 2).

To study a possible reason for the North-West to South-East preferential direction of fractures from a pure North-South one, we downloaded the heliocentric vector coordinates ($-r_{\rm ecl}$) of the astroid Bennu along its complete present orbit (440 days, arbitrarily starting from January 3$^{\rm rd}$, 2020) with a step of one day, using the IMCCE-MIRIADE ephemeris service (`https://vo.imcce.fr/webservices/miriade/`). We changed sign to the vector component in order to transfer the origin to Bennu and applied the following transformation:

$$r_{\rm ast} = \begin{pmatrix} \cos(90^\circ - \beta_H) & 0 & -\sin(90^\circ - \beta_H) \\ 0 & 1 & 0 \\ \sin(90^\circ - \beta_H) & 0 & \cos(90^\circ - \beta_H) \end{pmatrix} \begin{pmatrix} \cos\lambda_H & \sin\lambda_H & 0 \\ -\sin\lambda_H & \cos\lambda_H & 0 \\ 0 & 0 & 0 \end{pmatrix} r_{\rm ecl} \qquad (1)$$

where $r_{\rm ast}$ is the vector to the Sun in the asteroid-centric reference frame, λ_H=69.92° and β_H=–83.45°

are the ecliptic longitude and latitude of Bennu's rotation vector[4]. Next we calculated, for each point on the orbit, the latitude of the sub-solar point and the heliocentric distance and found that when Bennu is at perihelion the subsolar latitude is slightly negative, reaching -2.5° for heliocentric distances between 0.95 and 1 au. In addition, it is also possible hat Bennu had a smaller perihelion distance[44] and a different spin axis obliquity[1] in the past, resulting in stronger seasonal effects, which could had enhanced the deviation of the observed preferential fracture direction from a pure North-South one.

Thermal fatigue fracture propagation model

For modelling thermal fatigue fracture propagation, we used the analytical model developed through refs.[8,18,19]. We considered a cylindrical boulder of diameter $D = 2$ m and length $2L_x = 3$ m (Extended Data Fig. 8), resting on Bennu's equatorial surface and having its major axis (x) aligned along the preferential direction of fracture propagation (Fig. 2). The boulder contains a single planar surface fracture, whose length in the depth direction is denoted as a_z and full length in North-West to South-East direction is indicated as $2a_x$. The fracture's faces are normal to the North-East to South-West direction. The fracture vertical and horizontal growth rates are calculated separately following Paris law,

$$\frac{da_z}{dN} = C[\Delta K_{Iz}]^n \quad \text{and} \quad \frac{da_x}{dN} = C[\Delta K_{Ix}]^n, \tag{2}$$

where N denotes the number of thermal cycles, and n and C are the Paris' law exponent and pre-factor, whose values have been taken from a previous work[8]. The stress intensity factor excursions ΔK_I at the two fracture tips of interest – at depth and on the surface – are denoted as $\Delta K_{Iz} \equiv \Delta K_I(x = 0, y = 0, z = a_z)$ and $\Delta K_{Ix} \equiv \Delta K_I(x = a_x, y = 0, z = 0)$.

Following previous works[8,18,19], we first consider the problem of estimating the time it takes for a_z to reach a length equal to the boulder diameter. The stress intensity factor at the depth fracture tip (ΔK_{Iz}) has been previously studied[8,18,19] for the same circular boulder geometry defined here and thermal gradients resulting from diurnal temperature variations, but for different boulder diameters, temperature cycle periods (P), and diurnal temperature excursion (ΔT). We can thus solve the problem by using thermal fatigue scaling laws developed by ref.[18] and scale previous results to our case. Using equation 24 of ref.[18] for $D >> l_s$, where $l_s = \sqrt{\kappa P/(\pi \rho C_p)}$ is the diurnal heat penetration depth, κ is the thermal conductivity, ρ the material density, and C_p the specific heat capacity, we can write that

$$\frac{N}{N_{\rm ref}} = \left(\frac{D}{l_s}\right)^{n-1} \zeta^{1-n} (\Delta T)^{1.5(n-1)}, \tag{3}$$

where $\zeta = C^{\frac{1}{1-n}} E^{-1.25} \rho^{0.5} C_p^{0.5} \alpha^{-1.5}$ with E and α being the material's Young elastic modulus and thermal expansion coefficient, respectively, while $N_{\rm ref}$ is the number of temperature cycles to propagate a fracture to a length equal to the boulder diameter through a boulder with $D = l_s$. The value of l_s of ref.[8] can be calculated to be 6.4 cm for their carbonaceous chondrite case. For this length, their Fig. 1 gives a time of 3.5×10^3 years, corresponding to $N_{\rm ref} = 1.4 \times 10^6$ cycles, given their $P = 6$ hours, to grow a fracture from 30 μm to their l_s-value. Their ΔT can be read from their Extended Data Figure 2. For $D = l_s$ and $N = N_{\rm ref}$ in Eq. 3, we obtain $\zeta \sim$1300 K$^{1.5(1-n)}$. Equation 3 is then used to predict the N-value to grow a fracture $a_z = D =$2 m on Bennu: assuming $\Gamma = 370$ J m^{-2} s$^{-0.5}$ K^{-1} from ref.[11] as appropriate for Bennu's boulders, and C_p and ρ from ref.[8], we obtain $l_s =$ 5 cm. Hence, $D/l_s \sim 40$. For $\Delta T = 75$ K, which is roughly the average between the two curves of Fig. 2 of ref.[8], Eq. 3 gives $N \sim 7 \times 10^9$ cycles, corresponding to about 3.3 Myr for Bennu's rotation

period $P = 4.279$ h.

The stress intensity factor at the horizontal fracture tips (ΔK_{Ix}) can be approximated following the solution for a through fracture in a plate[45]:

$$\begin{aligned} K_{Ix} &= \frac{f\left(\frac{a_x}{L_x}\right)}{\sqrt{\pi a_x}} \int_0^{a_x} dx \frac{\sqrt{(a_x + x)}}{\sqrt{(a_x - x)}} \sigma_{yy}(x, y = 0, z = 0), \quad \text{with} \\ f\left(\frac{a_x}{L_x}\right) &= \left(1 - \frac{a_x}{L_x} + 0.326 \left(\frac{2a_x}{L_x}\right)^2\right) \left(1 - \frac{2a_x}{L_x}\right)^{-1/2}, \end{aligned} \tag{4}$$

where $f\left(\frac{a_x}{L_x}\right)$ is a correction factor to account for the finite dimension of the fracture relative to the plate. Following previous works[8,18,19], the thermal stress is governed by two contributing factors,

$$\sigma_{yy} = \sigma_{yy}^{l_s} + \sigma_{yy}^{\mathrm{TM}}, \tag{5}$$

where $\sigma_{yy}^{l_s}$ denotes macroscopic thermal stresses generated by the spatial variation of temperature through the depth of the boulder and $\sigma_{yy}^{\mathrm{TM}}$ denotes microscopic thermal stresses due to thermal expansion mismatch between different phases of the materials, e.g., inclusions and matrix. According to ref.[19], the peak microscopic thermal stresses in a carbonaceous chondrite-like material is $\sigma_{yy}^{\mathrm{TM}} = 0.884 \times K \Delta\alpha \Delta T_s$. Since the sign of the microscopic thermal stresses reverses at each chondrule-matrix interface, their contribution to the stress intensity factor is mostly canceled out after the fracture has traversed a few inclusions. Hence, the fatigue survival lifetime of a boulder with size $\gg$ than the typical distance and/or sizes of inclusions is most sensitive to macroscopic thermal stresses, with microscopic thermal stresses primarily accelerating the early fracture growth. According to ref.[19], the macroscopic thermal stresses due to the thermal gradient may be approximated as

$$\begin{aligned} \sigma_{yy}^{l_s} =& \frac{Q\alpha E \Delta T_s}{6(1-\nu)} \left(e^{\frac{-z}{l_s}} - \frac{l_s}{D}\left(1 - e^{\frac{-D}{l_s}}\right) + 3\frac{l_s}{D}\left(2\frac{z}{D} - 1\right)\left(2 - \left(2\frac{z}{D} + 1\right)\left(1 - e^{\frac{-D}{l_s}}\right)\right)\right) \\ \text{with } Q =& \max\left(\frac{1}{3}, \frac{3}{4}\frac{D + 4l_s}{D + 12l_s}\right), \end{aligned} \tag{6}$$

where Q is a geometric correction factor. Taking $\sigma_{yy}^{l_s}$ as a lower bound of $\sigma_{yy}(x, y = 0, z = 0)$, the corresponding lower bound of the peak lateral stress intensity factor may be analytically integrated:

$${}_{L-B}K_{Ix} = \sigma_{yy}^{l_s} \sqrt{\pi a_x} f\left(\frac{a_x}{L_x}\right). \tag{7}$$

This lower bound leads to an upper bound ($U - B$) on the time ${}_{U-B}t_f$ required to grow a lateral fatigue fracture from an initial length of a_{x0} to a final length a_{xf} from integration of Eq. 2, i.e.:

$${}_{U-B}t_f = PN_f = PC^{-1} \int_{a_{x0}}^{a_{xf}} da_x \left[{}_{L-B}K_{Ix}\right]^{-n}. \tag{8}$$

We evaluate iteratively the integral of Eq. 8 starting with $a_{x0} = 30$ μm, similarly to what was previously[8,18,19] done, and adding the time needed for the fracture to grow 1/10 of its length at each iteration, until $a_x \geq a_{xf} = L_x$. Equations 6 and 7 are evaluated at each iteration with $\alpha = 5 \times 10^{-6}$ K^{-1}, $\Delta T_s = 75$ K, $E = 10$ GPa following ref.[33], and $\nu = 0.2$, which is the average of the measured values reported[46] for CM type chondrite meteorites. We obtain ${}_{U-B}t_f \approx 40{,}000$ years for $2L_x = 3$ m.

We also use the same model to calculate the propagation as a function of time of a set of fractures

with a log-normal initial length distribution ranging between 10^{-6} and 4×10^{-4} m, which is similar to the distribution of micro fractures observed in meteorites[47]. We assign to each fracture a host boulder, whose size is randomly drawn from the distribution of ref.[7] with diameter smaller 30 m. The model proceed with a 10-year step during which each fracture is propagated by an amount given by Eq. 2. A fracture is not allowed to propagate longer than the size of the hosting boulder. Extended Data Fig. 9 shows the fracture length distribution at different epochs. The power-law slope of the cumulative distribution of fractures with lengths larger than 4 m for the after 50 and 100 kyr are of -2.1 and -2.2, respectively. This is consistent with the observed one.

Lastly, we provide some degree of uncertainty quantification for our model. This is done by studying the dependance of ${}_{U-B}t_f$ on model parameters by re-evaluating Eq. 8 as detailed before, but assigning a lower and upper value for each parameter as shown in Extended Data Tab. 1. The values of C and n were varied in ranges within which the model of ref.[8] would agree within a 100% relative error with the experimentally observed fracture growth in their work (see their Extended Data Fig. 9). The upper and lower bounds for E and ν are taken from ref.[46] and those for C_p, ρ, and α from ref.[48] (at a temperature of 270 K), which are obtained from laboratory measurements of CM carbonaceous chondrites. The upper bound for the thermal inertia Γ is also from ref.[48] (at 270 K), while its lower bound is that of the low thermal inertia unit of Bennu[11]. The range of amplitude of the temperature variation ΔT is reasonable for Bennu-like asteroids in near-Earth space[11,8]. Bennu's rotation period P could have been different than the current one in the past[15,30]. We thus halved and doubled the current P-value and took these as lower and upper bound, respectively. Finally we considered two very different initial values for fracture lengths which are quite extreme bounds for their typical sizes in CM carbonaceous chondrites[8]

Data Availability

Raw and calibrated OCAMS images, OLA data ancillary data are available via the Planetary Data System of NASA at `sbn.psi.edu/pds/resource/orex/`: ref.[49,50]. The OLA v20 shape model is available via the Small Body Mapping Tool at `sbmt.jhuapl.edu/`. The image mosaics used in this study are available from refs.[20,41]. Mosaic-FB3, mosaic-FB1, their respective .wcs files for SAOImage-DS9 and the fracture files (SAOImage-DS9 regions file) are available at `https://doi.org/10.5281/zenodo.6373668`. Source data are provided with this paper.

Code Availability

Fracture mapping was performed using the astronomical image display and visualisation tool SAOImageDS9 software, which is available at `cfa.harvard.edu/saoimageds9`, also using the XPA messaging system (`http://hea-www.harvard.edu/RD/xpa/index.html`). Codes to map fractures, calculate and plot their orientations, compute the fracture propagations are available at `https://doi.org/10.5281/zenodo.6373668`. The latter dataset includes also imaging mosaics FB1 and FB3 from their respective references.

Additional information

Correspondence and requests for materials should be addressed to Marco Delbo (`delbo@oca.eu`)

Reference list for the Methods section

[41] Golish, D. R. *et al.* Disk-resolved photometric modeling and properties of asteroid (101955) Bennu. *Icarus* **357**, 113724 (2021).

[42] Daly, M. G. *et al.* Hemispherical differences in the shape and topography of asteroid (101955) Bennu. *Science Advances* **6**, eabd3649 (2020).

[43] Bonnet, E. *et al.* Scaling of fracture systems in geological media. *Reviews of Geophysics* **39**, 347–383 (2001).

[44] Delbo, M. & Michel, P. Temperature History and Dynamical Evolution of (101955) 1999 RQ 36: A Potential Target for Sample Return from a Primitive Asteroid. *The Astrophysical Journal Letters* **728**, L42 (2011).

[45] Rooke, D. P. & Cartwright, D. J. *Compendium of stress intensity factors* (Great Britain Ministry of Defence. Procurement Executive, London H.M.S.O., 1976).

[46] Ibrahim, M. I. The Elastic Properties of Carbonaceous Chondrites. *MSc Thesis, Univ. Calgary* (2012).

[47] Bryson, K. L., Ostrowski, D. R. & Blasizzo, A. Meteorite flaws and scaling for atmospheric entry. *PSS* **164**, 85–90 (2018).

[48] Opeil, C. P., Britt, D. T., Macke, R. J. & Consolmagno, G. J. The surprising thermal properties of CM carbonaceous chondrites. *Meteoritics & Planetary Science* **55**, E1–E20 (2020).

[49] Rizk, B., Drouet d'Aubigny, C., Golish, D., DellaGiustina, D. N. & Lauretta, D. S. Origins, Spectral Interpretation, Resource Identification, Security, Regolith Explorer (OSIRIS-REx): OSIRIS-REx Camera Suite (OCAMS) Bundle (2019). NASA Planetary Data System, urn:nasa:pds:orex.ocams.

[50] Daly, M., Barnouin, O., Espiritu, R. & Lauretta, D. S. Origins, Spectral Interpretation, Resource Identification, Security, Regolith Explorer (OSIRIS-REx): OSIRIS-REx Laser Altimeter Bundle (2019). NASA Planetary Data System, urn:nasa:pds:orex.ola.

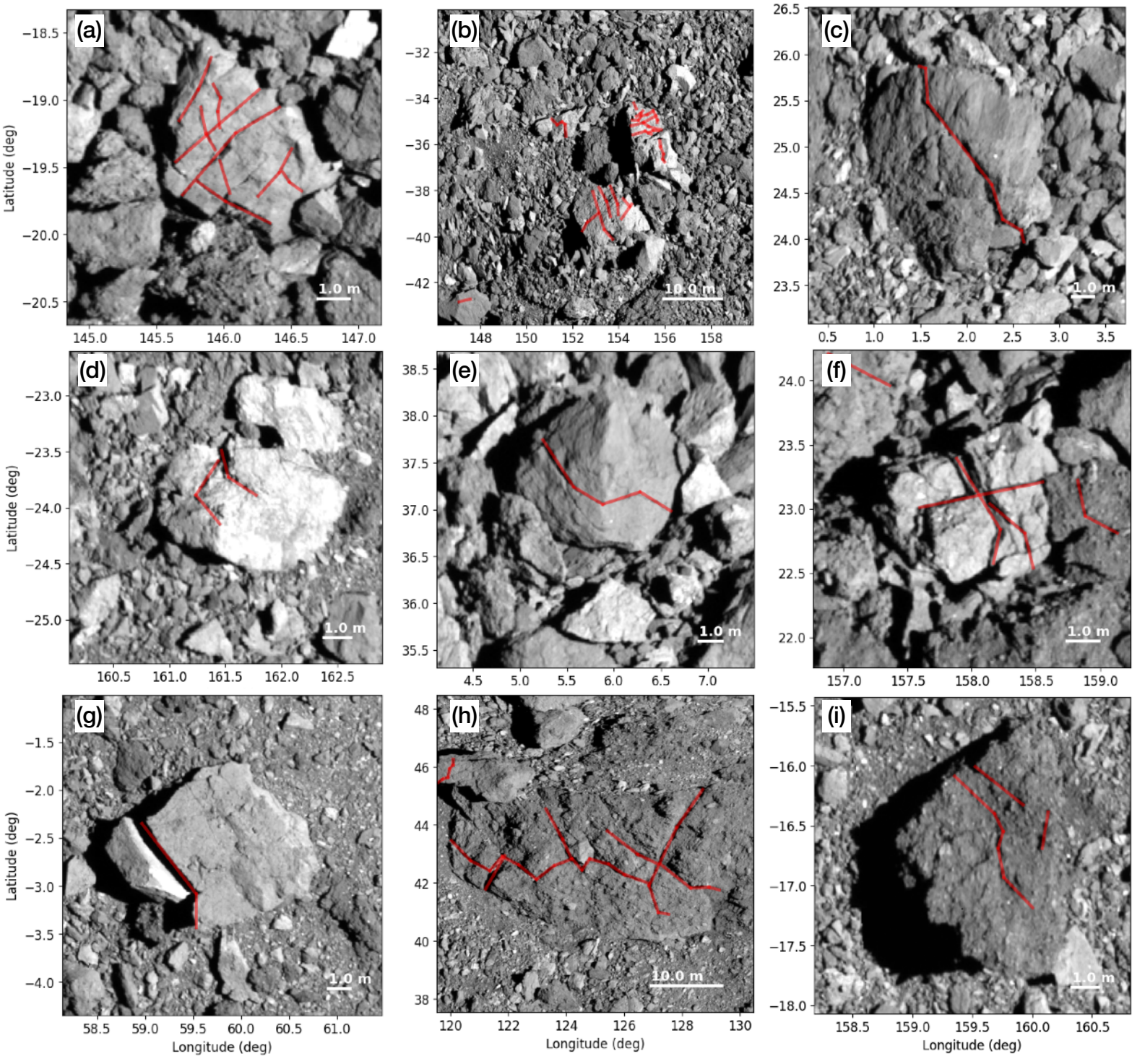
(a)
(b)
(c)
(d)
(e)
(f)
(g)
(h)
(i)
1.0 m
10.0 m
Latitude (deg)
Longitude (deg)

(a)

Latitude range: $15^o \leq \phi \leq 50^o$

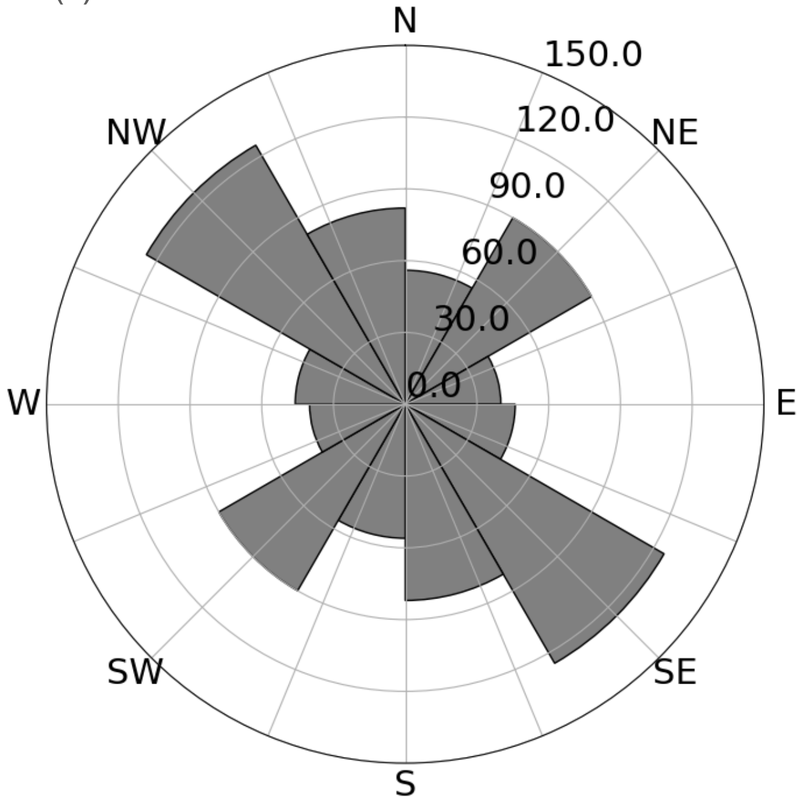

(b)

Latitude range: $-15^o \leq \phi \leq 15^o$

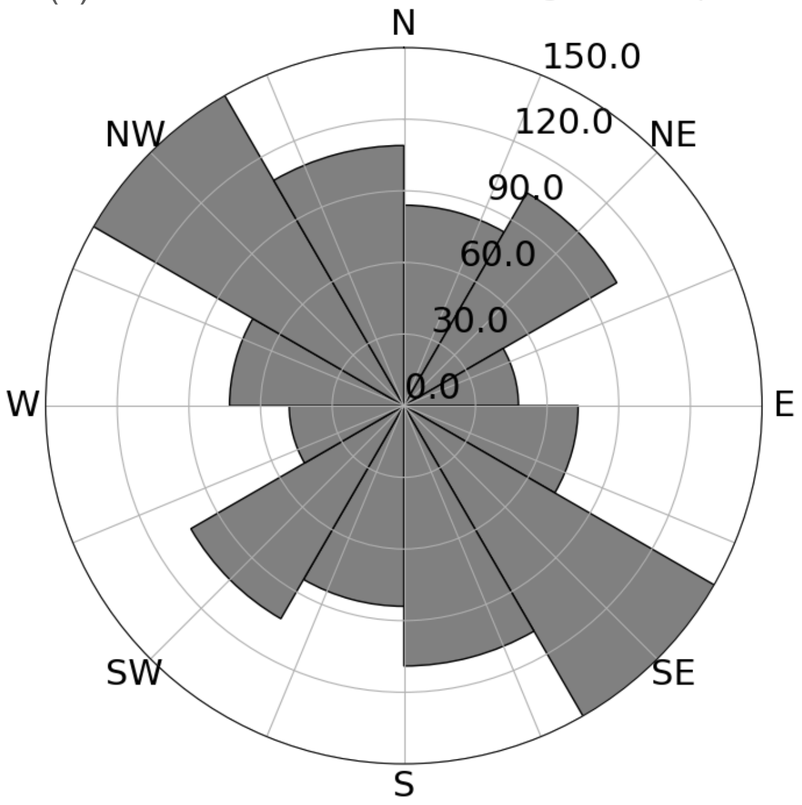

(c)

Latitude range: $-50^o \leq \phi \leq -15^o$

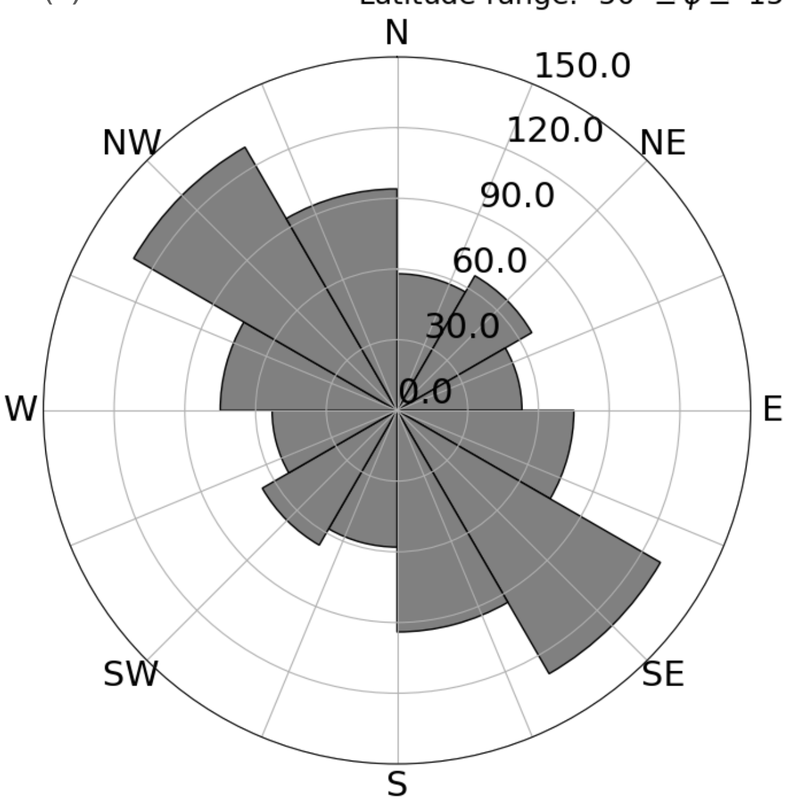

(d)

Latitude range: $15^o \leq \phi \leq 50^o$

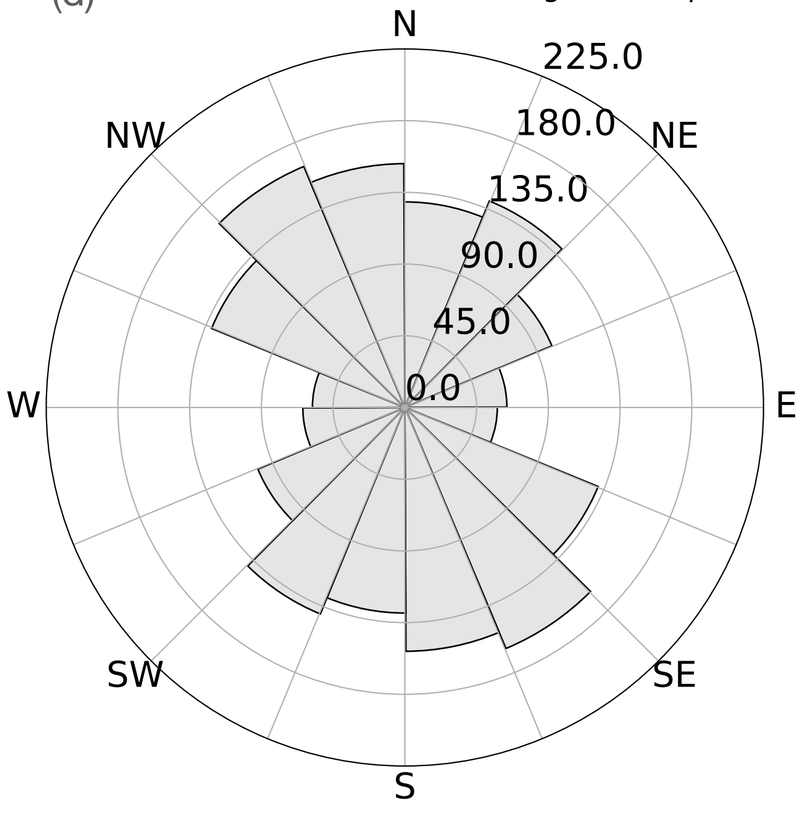

(e)

Latitude range: $-15^o \leq \phi \leq 15^o$

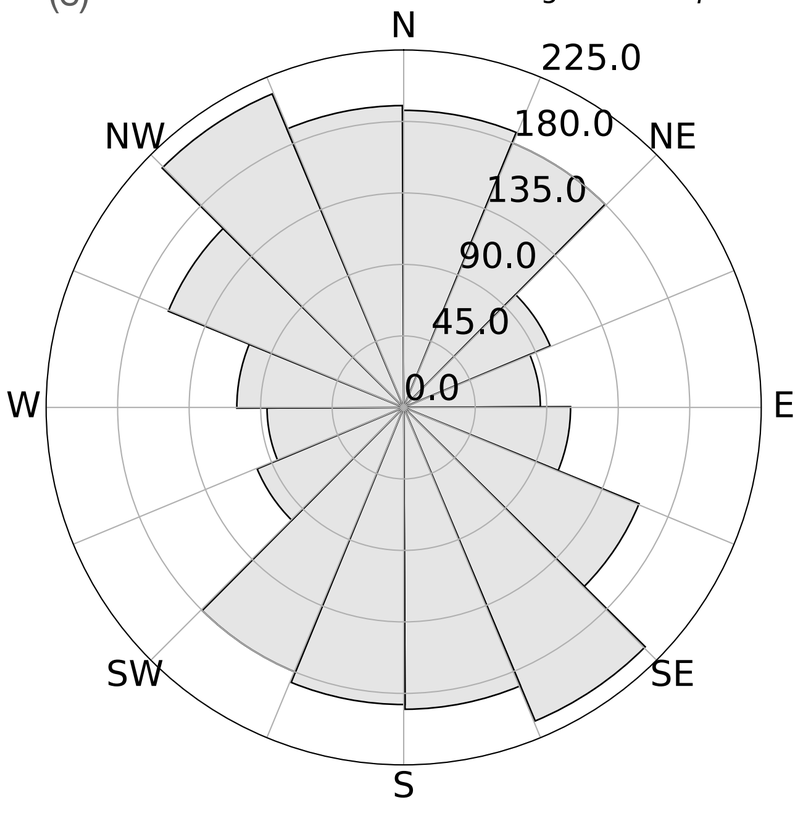

(f)

Latitude range: $-50^o \leq \phi \leq -15^o$

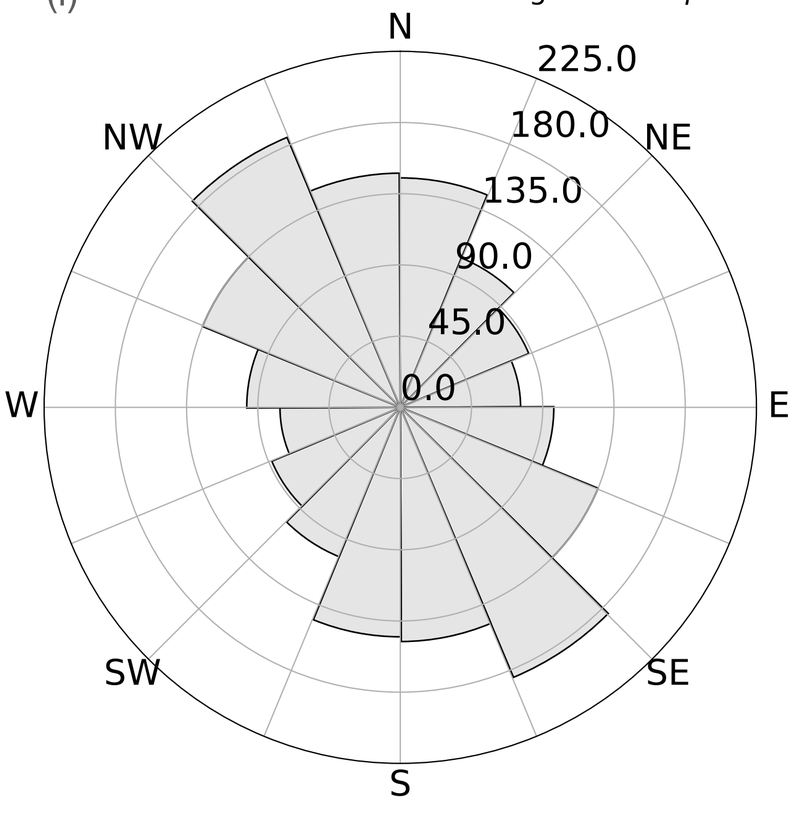

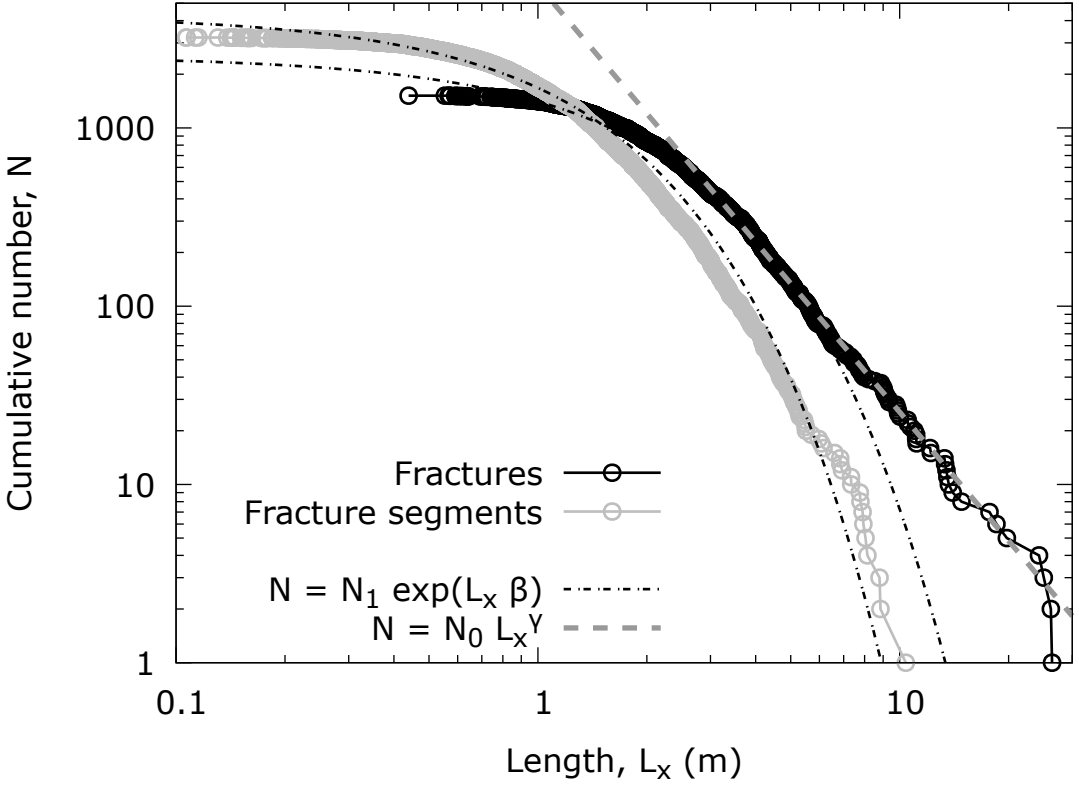
Cumulative number, N
1000
100
10
1
0.1
1
10
Length, L_x (m)
Fractures
Fracture segments
$N = N_1 \exp(L_x \beta)$
$N = N_0 L_x^Y$

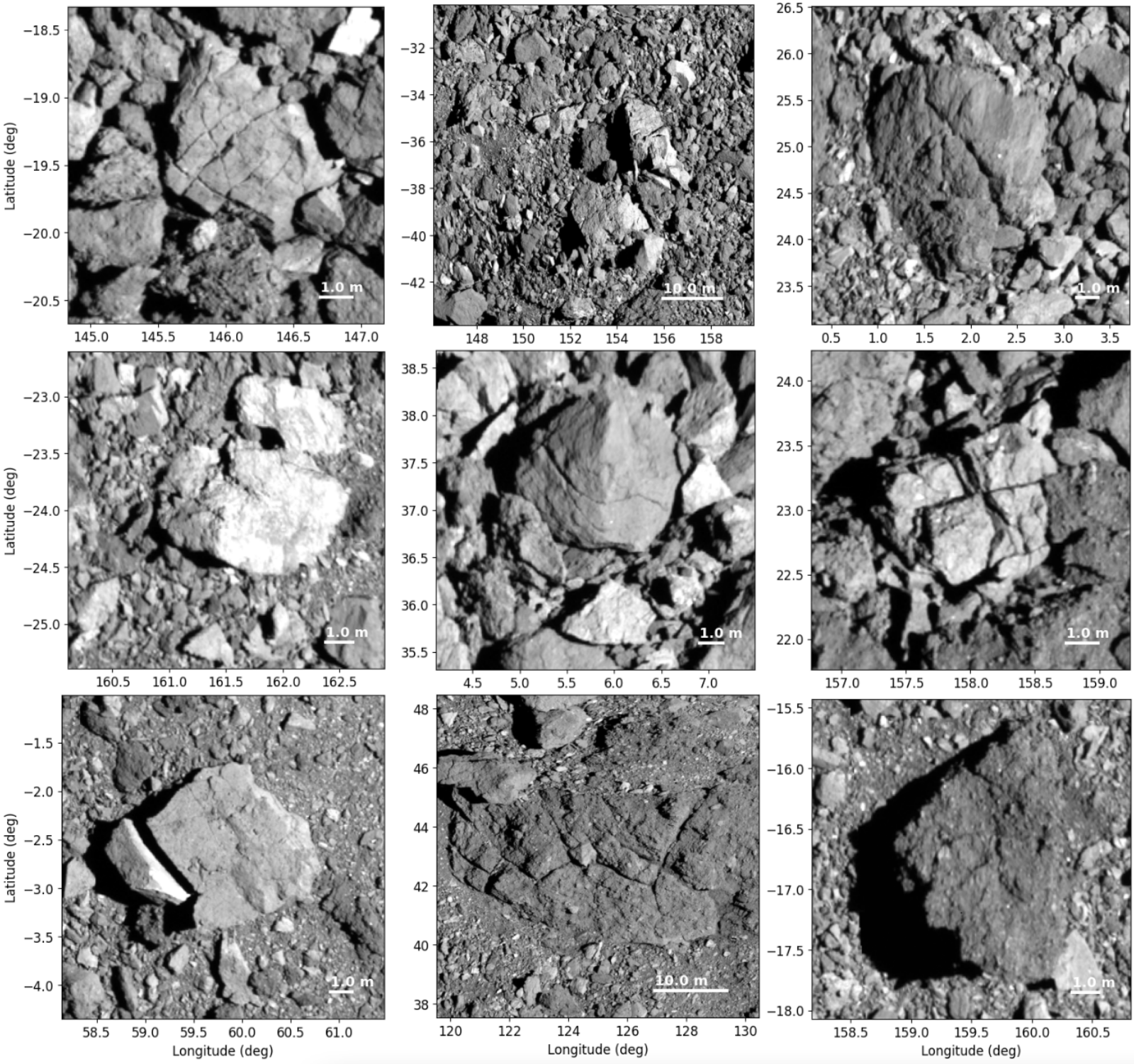
Latitude (deg)
−18.5
−19.0
−19.5
−20.0
−20.5
145.0
145.5
146.0
146.5
147.0
1.0 m
−32
−34
−36
−38
−40
−42
148
150
152
154
156
158
10.0 m
26.5
26.0
25.5
25.0
24.5
24.0
23.5
0.5
1.0
1.5
2.0
2.5
3.0
3.5
1.0 m
Latitude (deg)
−23.0
−23.5
−24.0
−24.5
−25.0
160.5
161.0
161.5
162.0
162.5
1.0 m
38.5
38.0
37.5
37.0
36.5
36.0
35.5
4.5
5.0
5.5
6.0
6.5
7.0
1.0 m
24.0
23.5
23.0
22.5
22.0
157.0
157.5
158.0
158.5
159.0
1.0 m
Latitude (deg)
−1.5
−2.0
−2.5
−3.0
−3.5
−4.0
58.5
59.0
59.5
60.0
60.5
61.0
Longitude (deg)
1.0 m
48
46
44
42
40
38
120
122
124
126
128
130
Longitude (deg)
10.0 m
−15.5
−16.0
−16.5
−17.0
−17.5
−18.0
158.5
159.0
159.5
160.0
160.5
Longitude (deg)
1.0 m

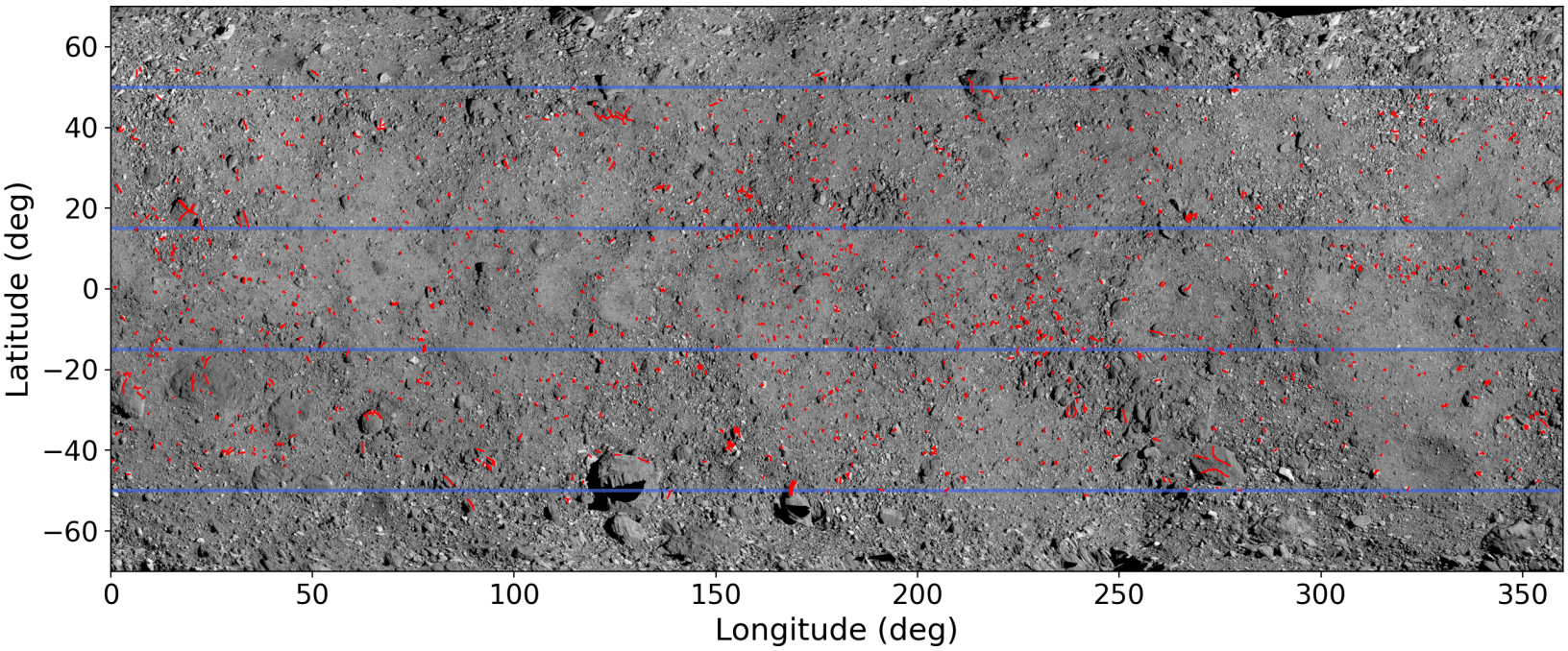
60
40
20
0
−20
−40
−60
Latitude (deg)
0
50
100
150
200
250
300
350
Longitude (deg)

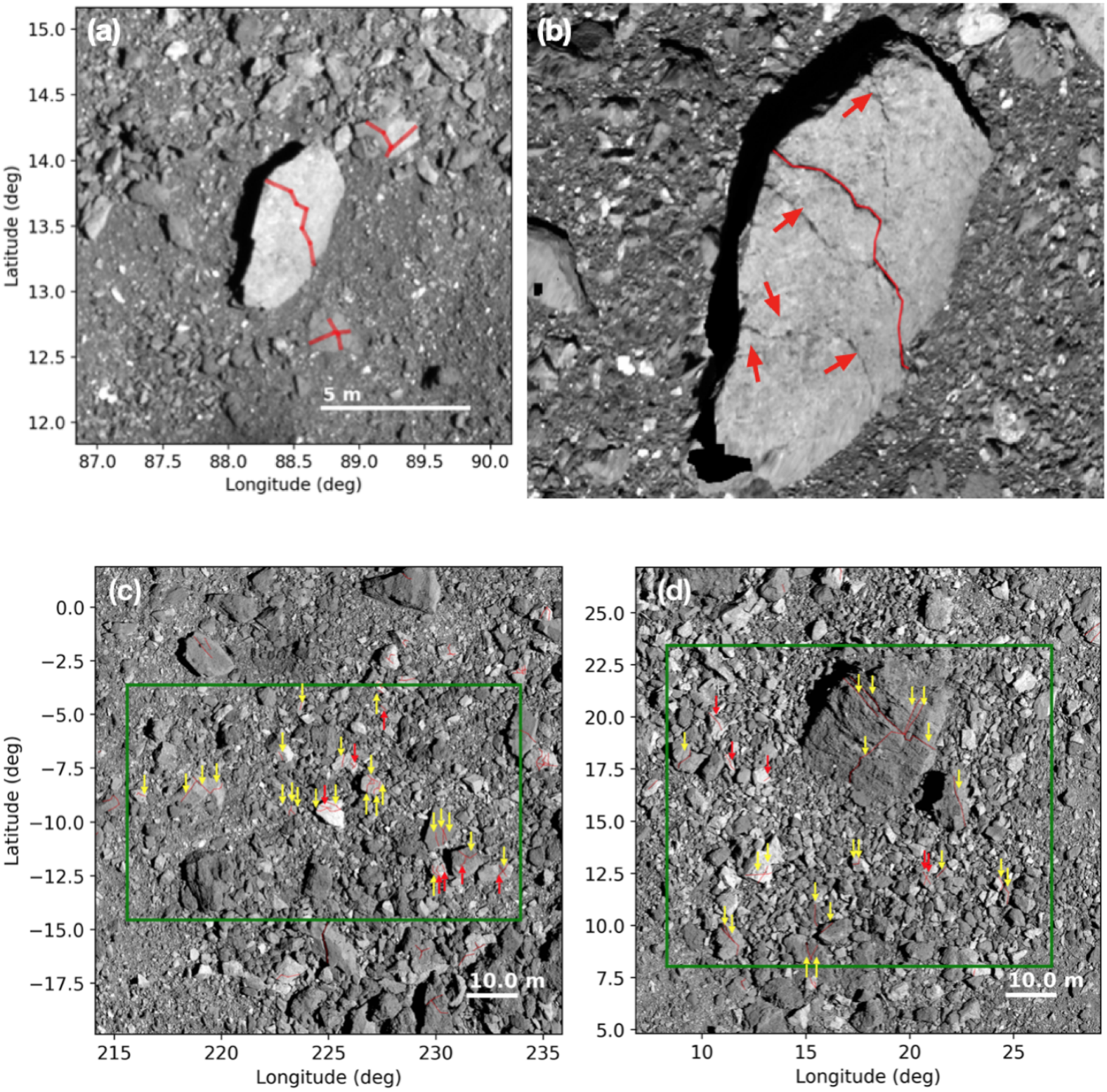
(a)
(b)
(c)
(d)
5 m
10.0 m
10.0 m
Latitude (deg)
Longitude (deg)
15.0
14.5
14.0
13.5
13.0
12.5
12.0
87.0
87.5
88.0
88.5
89.0
89.5
90.0
0.0
−2.5
−5.0
−7.5
−10.0
−12.5
−15.0
−17.5
215
220
225
230
235
25.0
22.5
20.0
17.5
15.0
12.5
10.0
7.5
5.0
10
15
20
25

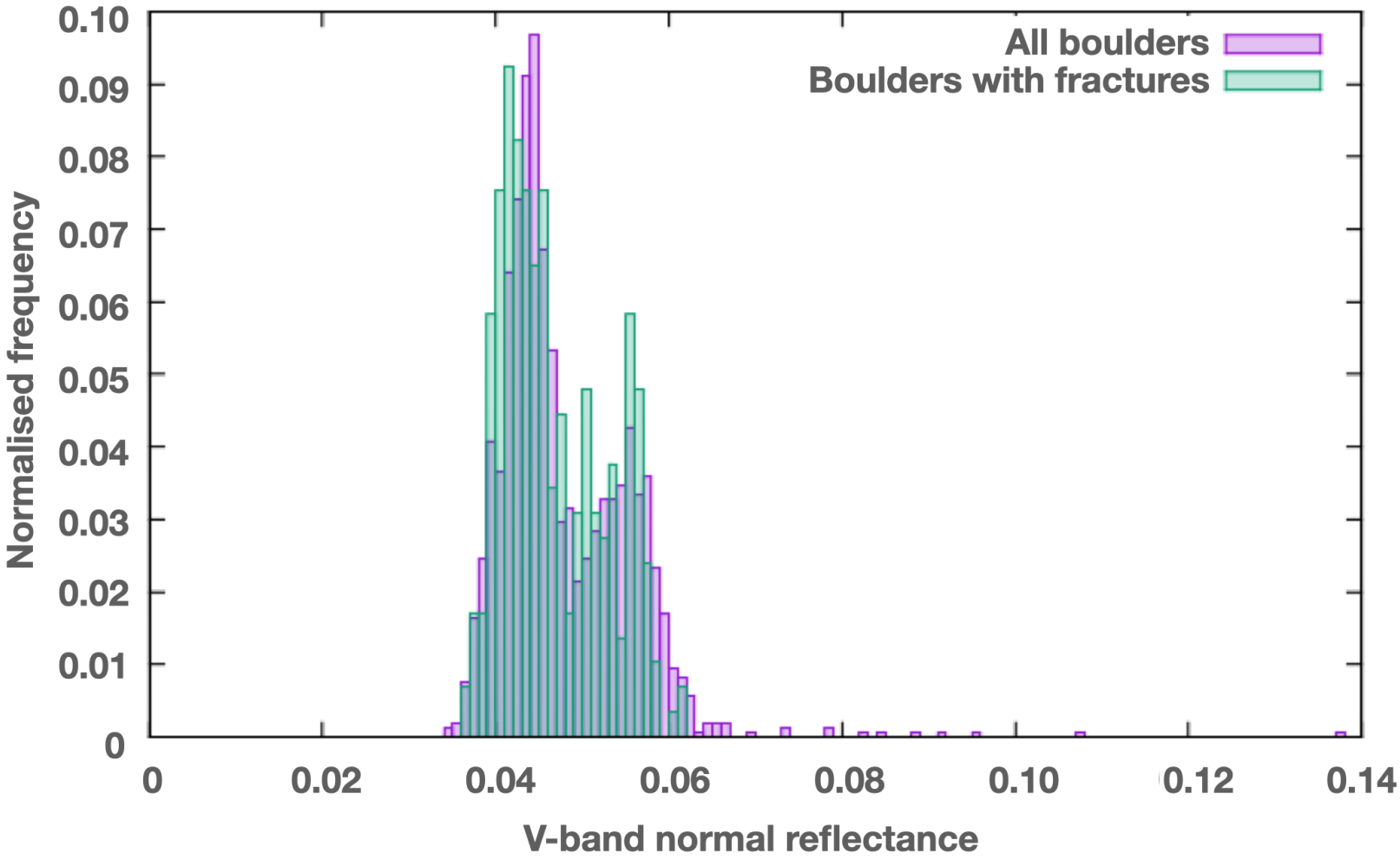
All boulders
Boulders with fractures
Normalised frequency
0.10
0.09
0.08
0.07
0.06
0.05
0.04
0.03
0.02
0.01
0
0
0.02
0.04
0.06
0.08
0.10
0.12
0.14
V-band normal reflectance

(a)

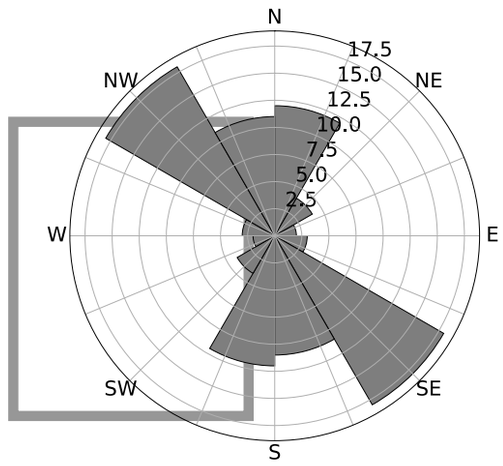

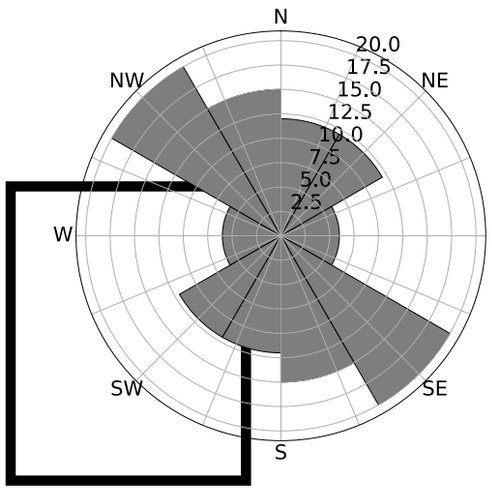

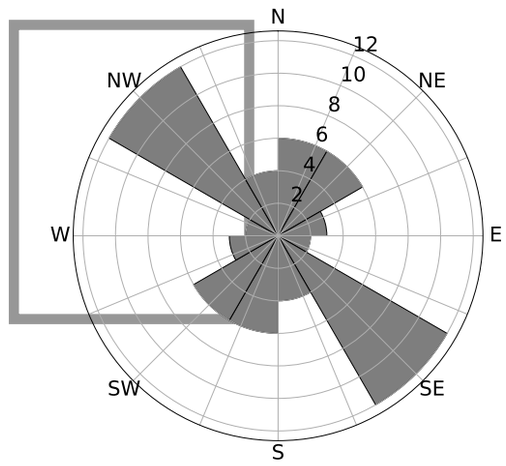

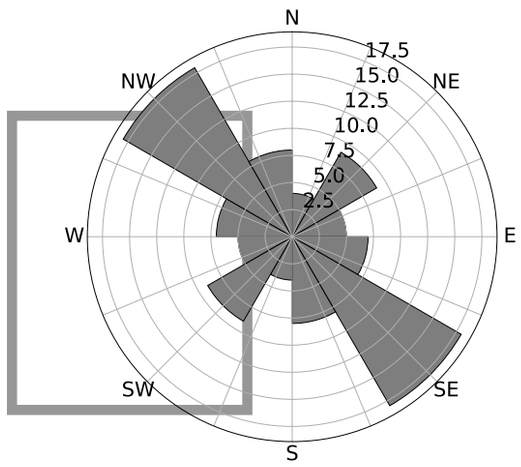

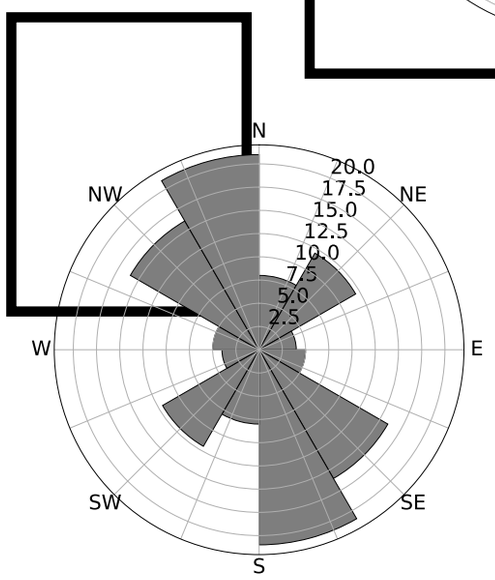

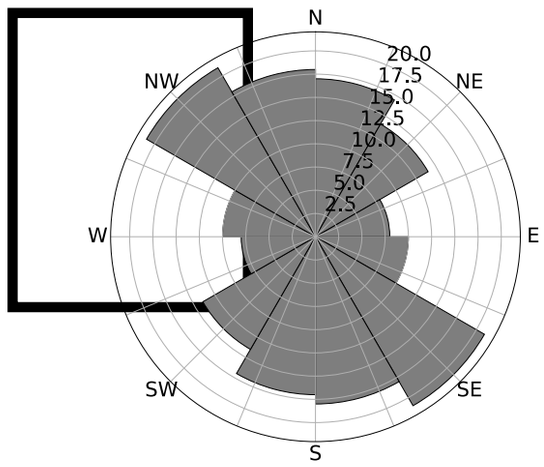

Latitude (deg)

60 50 40 30 20 10 0 −10 −20 −30 −40 −50 −60 −70

0 30 60 90 120 150 180 210 240 270 300 330 360

Longitude (deg)

(b)

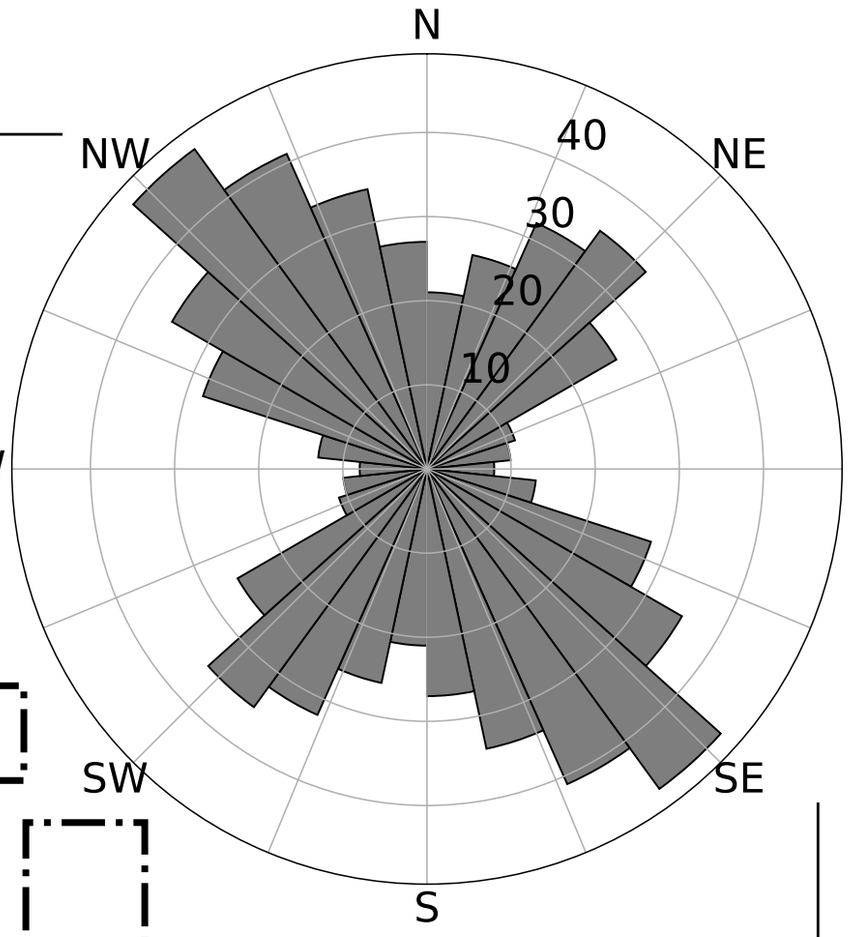

Latitude (deg)

60 50 40 30 20 10 0 −10 −20 −30 −40 −50 −60 −70

0 30 60 90 120 150 180 210 240 270 300 330 360

Longitude (deg)

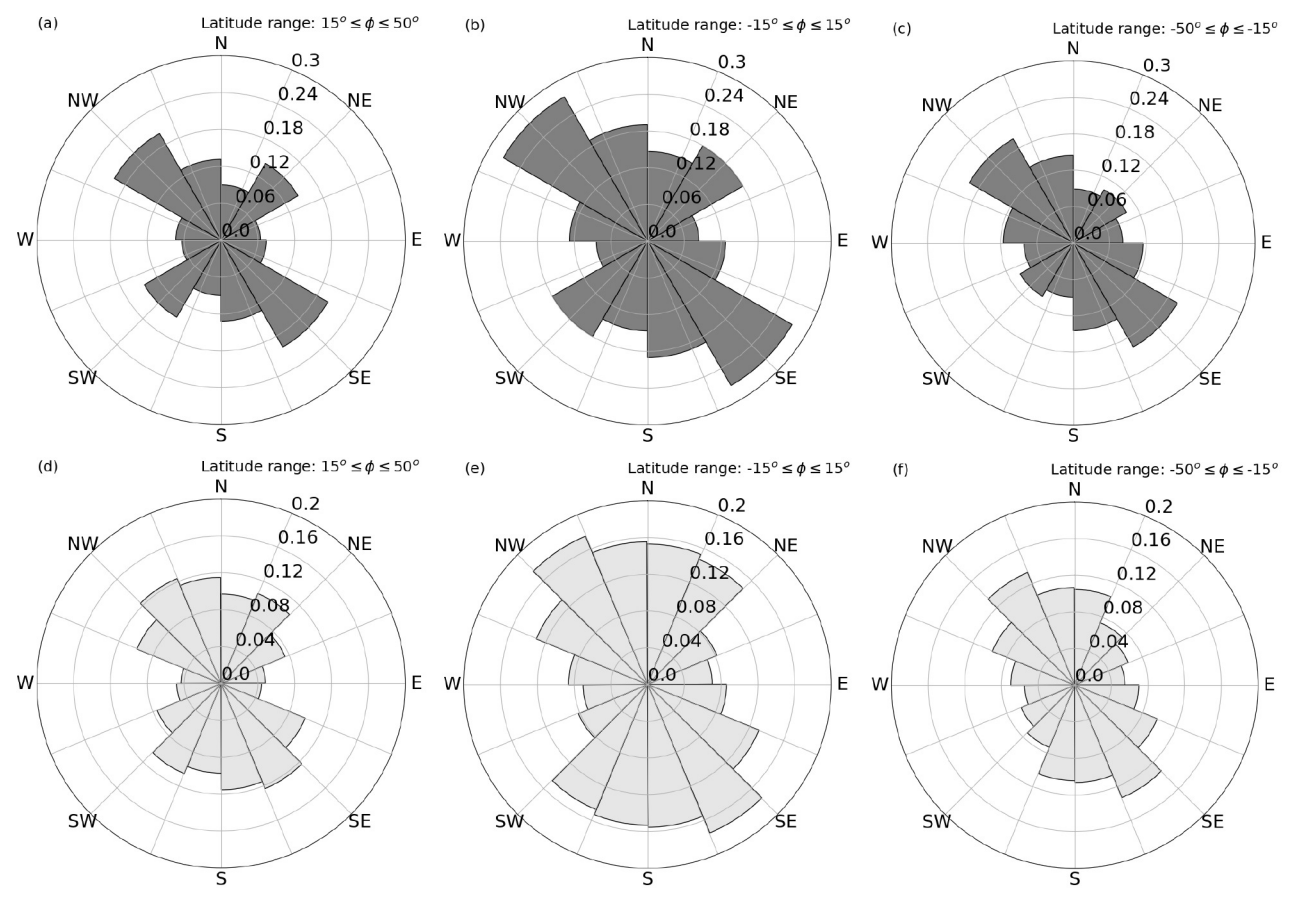
(a)
Latitude range: 15° ≤ ϕ ≤ 50°
(b)
Latitude range: -15° ≤ ϕ ≤ 15°
(c)
Latitude range: -50° ≤ ϕ ≤ -15°
(d)
Latitude range: 15° ≤ ϕ ≤ 50°
(e)
Latitude range: -15° ≤ ϕ ≤ 15°
(f)
Latitude range: -50° ≤ ϕ ≤ -15°
N
NE
E
SE
S
SW
W
NW
0.0
0.06
0.12
0.18
0.24
0.3
0.04
0.08
0.16
0.2

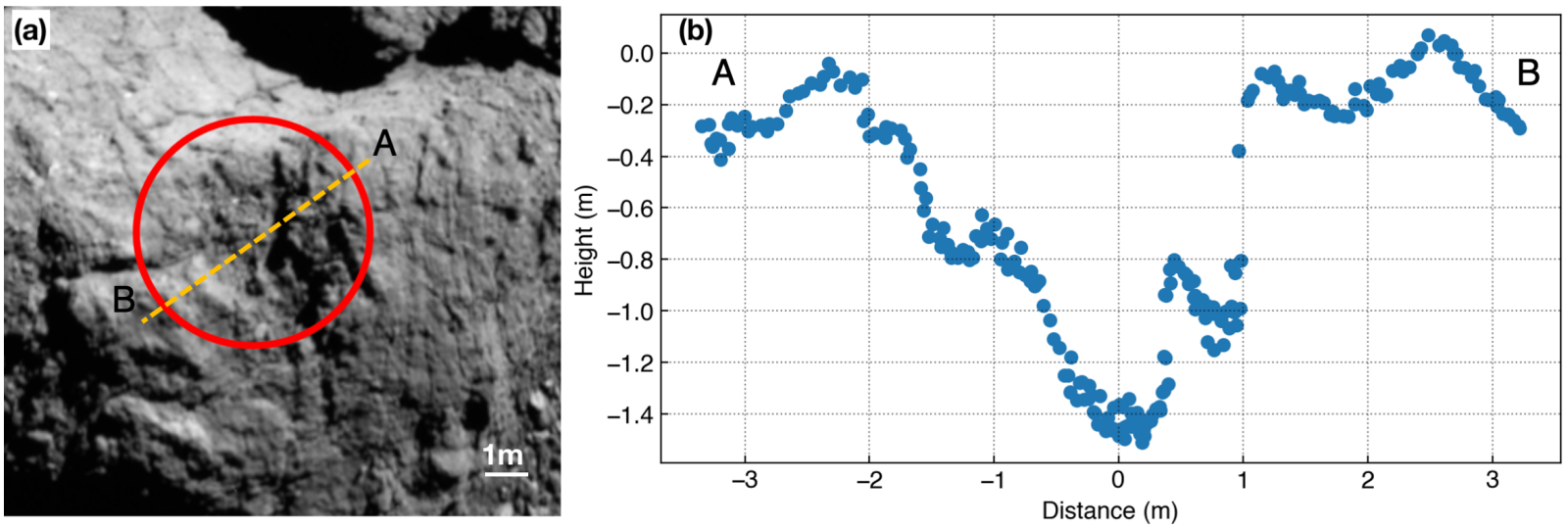
(a)
A
B
1m
(b)
A
B
0.0
−0.2
−0.4
−0.6
−0.8
−1.0
−1.2
−1.4
Height (m)
−3
−2
−1
0
1
2
3
Distance (m)

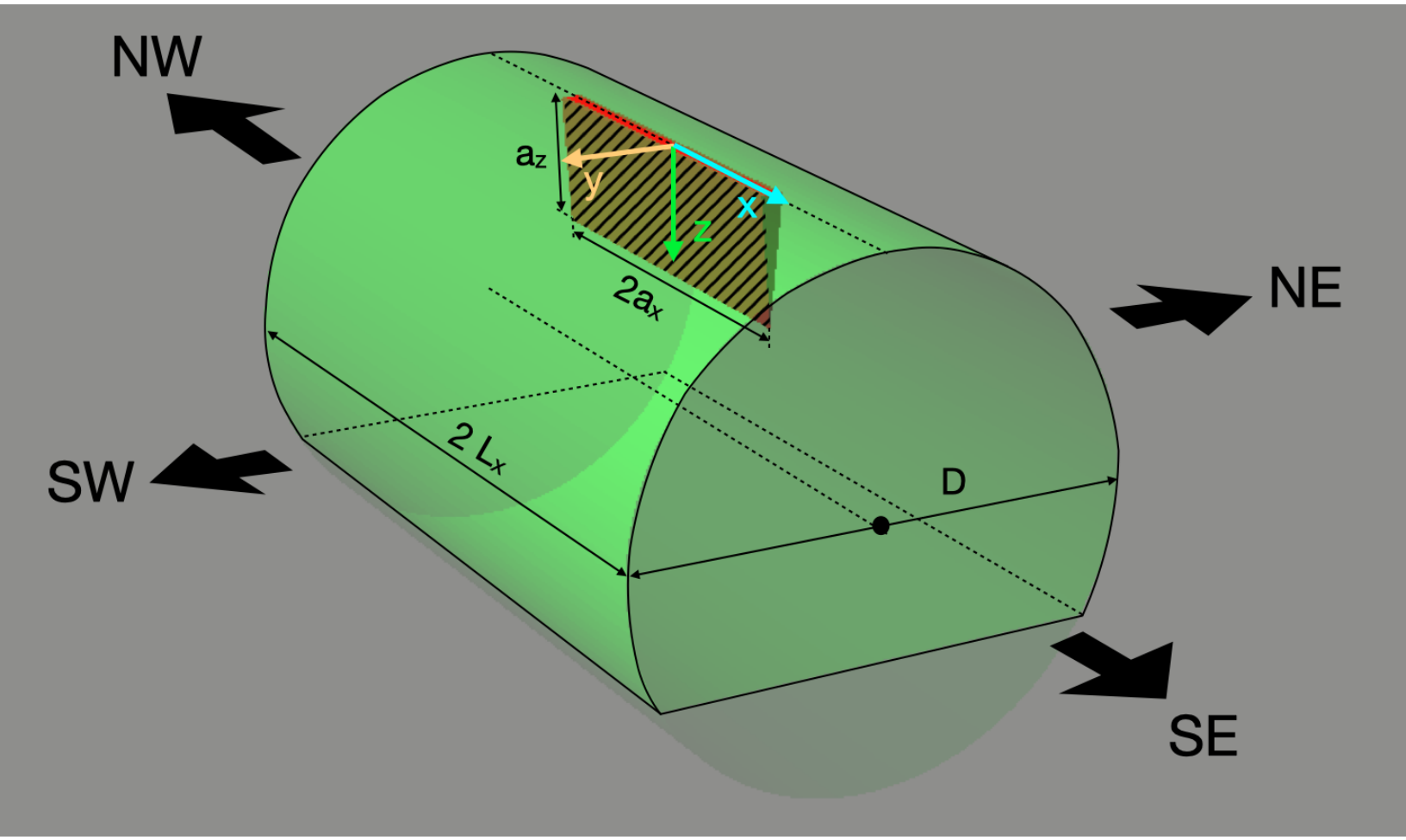
NW
NE
SW
SE
a_z
y
z
x
$2a_x$
$2L_x$
D

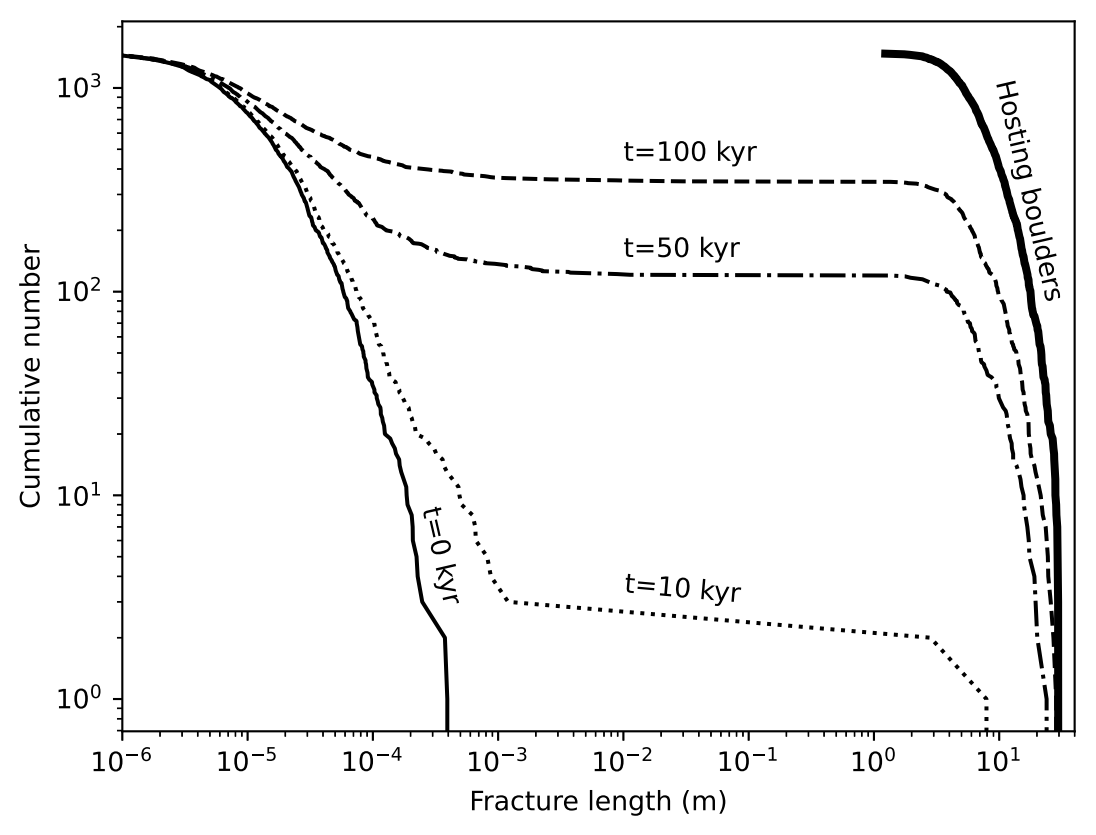
Cumulative number
10^3
10^2
10^1
10^0
10^{-6}
10^{-5}
10^{-4}
10^{-3}
10^{-2}
10^{-1}
10^0
10^1
Fracture length (m)
t=100 kyr
t=50 kyr
t=10 kyr
t=0 kyr
Hosting boulders

Parameter	Lower	Upper	Units	${}_{U-B}t_f$ (lower) 10^3 years	${}_{U-B}t_f$ (upper) 10^3 years
Paris' law pre-factor, C	3×10^{-5}	1×10^{-3}	$\mathrm{m}\,[\mathrm{MPa}\,\sqrt{\mathrm{m}}]^{-n}$	400	12
Paris' law exponent, n	3.3	4.3	-	3	380
Young modulus, E	4.5	25	GPa	4	400
Poisson ratio, ν	0.07	0.28	-	73	27
Thermal expansion coefficient, α	2×10^{-6}	8×10^{-6}	K^{-1}	290	7
Heat capacity, C_p	800	1200	$\mathrm{J\ kg^{-1}\ K^{-1}}$	44	39
Density, ρ	2040	2310	m^3	42	36
Thermal inertia, Γ	190	3000	$\mathrm{J\ m^{-2}\ s^{-0.5}\ K^{-1}}$	36	180
Diurnal temperature amplitude, ΔT	50	120	K	150	50
Rotation period, P	2.139	8.558	h	19	90
Initial fracture length, a_{x0}	1×10^{-6}	1×10^{-3}	m	300	3